Computers & Fluids 61 (2012) 46–63

Contents lists available at SciVerse ScienceDirect

Computers & Fluids

journal homepage: www.elsevier.com/locate/compfluid

A high-order finite-difference algorithm for direct computation of aerodynamic sound

F. Daude [a], J. Berland [a], T. Emmert [a], P. Lafon [a,*], F. Crouzet [a], C. Bailly [b,c]

[a] LaMSID, UMR EDF/CNRS/CEA 2832, 1 Av. du Général De Gaulle, 92141 Clamart, France
[b] LMFA, UMR CNRS 5509, 36 Av. Guy de Collongue, 69134 Ecully, France
[c] Institut Universitaire de France, 103 Bvd Saint-Michel, 75005 Paris, France

ARTICLE INFO

Article history:
Received 16 February 2011
Received in revised form 29 July 2011
Accepted 24 August 2011
Available online 19 September 2011

Keywords:
Computational AeroAcoustics
Large-eddy simulation
High-order schemes
Overset grids

ABSTRACT

A high-order finite-difference algorithm is proposed in the aim of performing LES calculations for CAA applications. The subgrid scale dissipation is performed by the explicit high-order numerical filter used for numerical stability purpose. A shock-capturing non-linear filter is also used to deal with compressible discontinuous flows. In order to tackle complex geometries, an overset-grid approach is used. High-order interpolations make possible the communication between overlapping domains. The whole algorithm is first validated on canonical flow problems to illustrate both its properties for shock-capturing as well as for accurate wave propagation. Then, the influence of the multi-domain approach on the high-order spatial accuracy is assessed. Finally, a rod-airfoil configuration is studied to highlight the potential of the proposed algorithm to deal with multi-scale aeroacoustic applications.

1. Introduction

In a wide range of technical fields such as aircrafts, automotive engineering, trains, turbomachinery, power plants, turbulent flows generate noise and noise often interacts with flows through a feedback loop. Particularly in ducted configurations, strong acoustics feedback mechanisms are involved. For example, a pure tone phenomenon has been observed on nuclear power stations due to an aeroacoustic coupling in an open gate valve [1]. In the same way, strong interactions between shock oscillations, internal aerodynamic noise and acoustic duct modes are often observed in confined flows but are undesirable to prevent structural excitation and fatigue [2]. It is well known that non-linear interactions between the turbulent flow and the acoustic field produce undesirable high pressure levels [3]. They are a source of noise pollution which is a major environmental issue. To numerically predict aeroacoustic coupling, the calculation of both the unsteady flow and the associated sound must be performed in the same computation. This is referred as Direct Noise Computation (DNC) in the literature of Computational AeroAcoustics (CAA) [4]. Using DNC is a powerful way to identify the fluid mechanism contributing to the sound production and therefore, a useful tool to reduce the noise radiation.

The large disparity in the characteristic scales of the acoustic and the flow fluctuations, and the need to accurately resolve high wavenumber fluctuations require the use of numerical methods with minimal dissipation and dispersion errors [3]. Traditional second-order accurate methods are known to be too dissipative for linear propagation. A recent review of high-order methods can be found in [5]. Three different families of high-order methods can be encountered in the literature: Weighted Essentially Non Oscillatory (WENO) [6], Discontinuous Galerkin (DG) [7] and finite-difference (FD) methods. Due to their simplicity, the high-order finite-difference methods are considered in this paper. The implicit compact [8] or the explicit DRP (Dispersion-Preserving-Relation) [9] or optimized [10] finite-difference schemes in conjunction with selective filter are an efficient and attractive way to provide low dispersive and low dissipative methods. However, these procedures, in most early works, were limited to academic cases with single domain and Cartesian grids. With the use of general curvilinear coordinates transformation [11,12], these methods can now be applied on more complex geometries. In the same way, high-order overset-grid approaches [13–15] are developed to handle realistic configurations including multiple bodies. Another advantage of the overset-grid strategy is the use of multi-block meshes which can be used on massively parallel computing platforms [16]. In addition, transonic compressible turbulent flows are characterized by the presence of shock waves which interact with turbulence. A shock-capturing scheme must also be implemented but implies the introduction of numerical dissipation. The development of numerical algorithms that capture discontinuities and also resolve both the scales of turbulence and the generated acoustic waves in compressible turbulent flows remains a significant challenge. In order

* Corresponding author. Tel.: +33 1 47 65 37 08; fax: +33 1 47 65 36 92.
E-mail address: philippe.lafon@edf.fr (P. Lafon).

0045-7930/$ - see front matter © 2011 Elsevier Ltd. All rights reserved.
doi:10.1016/j.compfluid.2011.08.017

to treat industrial configurations, a new numerical code called *Code_Safari* (Simulation of Aeroacoustic Flows And Resonance and Interaction) has been developed.

This paper is organized as follows. After having briefly presented the governing equations in Section 2, the proposed algorithm based on high-order finite-difference schemes in conjunction with optimized high-order low-pass spatial filters is presented in Section 3. To highlight the spectral behavior of this algorithm, a linear analysis is performed on the global numerical method including both spatial, temporal discretizations and selective filter. The shock-capturing procedure is performed via a non-linear filter after the time integration. A special attention is paid on the shock-detector which is the key issue in the preservation of the algorithm spectral behavior. In order to tackle complex geometries as multiple bodies, the employed overset-grid strategy with high-order Lagrangian interpolation is presented and a linear analysis of the interpolation error is given. The ability of the present algorithm to capture discontinuities in canonical 1-D and 2-D problems without damaging its initial propagation properties is discussed in Section 4. Afterwards, it is shown that the multi-domain strategy does not corrupt the algorithm characteristics via numerical examples. Finally, a direct computation of the aerodynamic sound is performed on the realistic rod-airfoil case to highlight the potential of the present solver.

2. Governing equations

2.1. Fluid dynamics

The three-dimensional Navier–Stokes equations are expressed in Cartesian coordinates for a viscous compressible Newtonian flow. After the application of a general curvilinear transformation $(x,y,z) \to (\xi,\eta,\zeta)$ as in [17,18], these equations are written in the following strong conservative form:

$$\partial_t \widehat{\boldsymbol{U}} + \partial_\xi\left(\boldsymbol{F}_\xi - \boldsymbol{F}_\xi^v\right) + \partial_\eta\left(\boldsymbol{F}_\eta - \boldsymbol{F}_\eta^v\right) + \partial_\zeta\left(\boldsymbol{F}_\zeta - \boldsymbol{F}_\zeta^v\right) = \boldsymbol{0}. \tag{1}$$

$\widehat{\boldsymbol{U}} = \boldsymbol{U}/J$ where $\boldsymbol{U} = (\rho, \rho\boldsymbol{u}, \rho e)^T$ is the vector of conservative variables, ρ is the density, $\boldsymbol{u} = (u,v,w)^T$ the Cartesian velocity vector, e is the total specific energy:

$$\rho e = \frac{p}{\gamma - 1} + \frac{1}{2}\rho\|\boldsymbol{u}\|^2,$$

where p is the pressure, γ the specific heat ratio and J the Jacobian of the coordinate transformation $(x,y,z) \to (\xi,\eta,\zeta)$.

$\boldsymbol{F}_\xi$, $\boldsymbol{F}_\eta$ and $\boldsymbol{F}_\zeta$ are the inviscid flux-vectors which can be expressed as:

$$\boldsymbol{F}_\xi = \frac{1}{J}\begin{pmatrix} \rho\Theta_\xi \\ \rho\boldsymbol{u}\Theta_\xi + p\nabla\xi \\ (\rho e + p)\Theta_\xi \end{pmatrix}, \quad \boldsymbol{F}_\eta = \frac{1}{J}\begin{pmatrix} \rho\Theta_\eta \\ \rho\boldsymbol{u}\Theta_\eta + p\nabla\eta \\ (\rho e + p)\Theta_\eta \end{pmatrix},$$
$$\boldsymbol{F}_\zeta = \frac{1}{J}\begin{pmatrix} \rho\Theta_\zeta \\ \rho\boldsymbol{u}\Theta_\zeta + p\nabla\zeta \\ (\rho e + p)\Theta_\zeta \end{pmatrix}.$$

The contra-variant velocity components Θ_ξ, Θ_η and Θ_ζ are defined as:

$$\Theta_\xi = \boldsymbol{u}\cdot\nabla\xi, \quad \Theta_\eta = \boldsymbol{u}\cdot\nabla\eta \quad \text{and} \quad \Theta_\zeta = \boldsymbol{u}\cdot\nabla\zeta.$$

with $\nabla\xi = (\xi_x, \xi_y, \xi_z)^T$. The quantities ξ_x, ξ_y, ξ_z, η_x, η_y, η_z, ζ_x, ζ_y and ζ_z designate the spatial metrics where the subscripts denote the partial derivatives.

$\boldsymbol{F}_\xi^v$, $\boldsymbol{F}_\eta^v$ and $\boldsymbol{F}_\zeta^v$ are the viscous flux-vectors which can be expressed as:

$$\boldsymbol{F}_\xi^v = \frac{1}{J}\begin{pmatrix} 0 \\ \boldsymbol{\mathcal{V}}_\xi \\ \boldsymbol{u}\cdot\boldsymbol{\mathcal{V}}_\xi - \boldsymbol{q}\cdot\nabla\xi \end{pmatrix}, \quad \boldsymbol{F}_\eta^v = \frac{1}{J}\begin{pmatrix} 0 \\ \boldsymbol{\mathcal{V}}_\eta \\ \boldsymbol{u}\cdot\boldsymbol{\mathcal{V}}_\eta - \boldsymbol{q}\cdot\nabla\eta \end{pmatrix},$$
$$\boldsymbol{F}_\zeta^v = \frac{1}{J}\begin{pmatrix} 0 \\ \boldsymbol{\mathcal{V}}_\zeta \\ \boldsymbol{u}\cdot\boldsymbol{\mathcal{V}}_\zeta - \boldsymbol{q}\cdot\nabla\zeta \end{pmatrix}.$$

The vectors $\boldsymbol{\mathcal{V}}_\xi$, $\boldsymbol{\mathcal{V}}_\eta$ and $\boldsymbol{\mathcal{V}}_\zeta$ are defined as: $\boldsymbol{\mathcal{V}}_\xi = \boldsymbol{\mathcal{D}}\cdot\nabla\xi$, $\boldsymbol{\mathcal{V}}_\eta = \boldsymbol{\mathcal{D}}\cdot\nabla\eta$ and $\boldsymbol{\mathcal{V}}_\zeta = \boldsymbol{\mathcal{D}}\cdot\nabla\zeta$.

$\boldsymbol{\mathcal{D}}$ is the viscous stress tensor and $\boldsymbol{q}$ the heat flux-vector which are defined as:

$$\boldsymbol{\mathcal{D}} = \mu\left[\nabla\boldsymbol{u} + \nabla\boldsymbol{u}^T - \frac{2}{3}(\nabla\cdot\boldsymbol{u})\boldsymbol{I_d}\right] \quad \text{and} \quad \boldsymbol{q} = -k\nabla T$$

with μ the dynamic shear viscosity given by the Sutherland's law, k the thermal conductivity given by the Fourier's law, $T = p/(\rho R)$ the temperature and R the gas constant.

2.2. Geometrical conservation

With the strong-conservation form in Eq. (1), the following relation must be satisfied numerically to ensure free-stream preservation when a finite-difference discretization is used [12]:

$$\partial_\xi\left(\frac{1}{J}\nabla\xi\right) + \partial_\eta\left(\frac{1}{J}\nabla\eta\right) + \partial_\zeta\left(\frac{1}{J}\nabla\zeta\right) = \boldsymbol{0} \tag{2}$$

This relation corresponds to the Surface Conservation Law (SCL) [19]. Usually, the SCL is numerically violated since numerical spatial operators are not commutative in contrast to their corresponding analytical ones. To enforce the numerical metric error cancellation and thus, to ensure the free-stream preservation, the spatial metrics are expressed in the conservative form proposed by Thomas and Lombard [20]:

$$\begin{cases} \frac{1}{J}\xi_x = (y_\eta z)_\zeta - (y_\zeta z)_\eta \\ \frac{1}{J}\xi_y = (y_\zeta z)_\xi - (y_\xi z)_\zeta \\ \frac{1}{J}\xi_z = (y_\xi z)_\eta - (y_\eta z)_\xi \end{cases} \tag{3}$$

Visbal and Gaitonde [12] have studied the influence of the metric evaluation errors for high-order compact finite-difference schemes. Using the conservative form proposed by Thomas and Lombard [20] and computing the spatial derivatives with the same discretization operator used for the flux derivatives, largely decrease this error. This is done in what follows.

3. Numerical method

3.1. Spatial discretization

The temporal integration is split from the spatial discretization. First derivatives at interior grid points are determined using N-point high-order centered finite-difference schemes:

$$\partial_\xi f_{i,j,k} \approx \frac{1}{\Delta\xi}\sum_{m=1}^{N} s_m\left(f_{i+m,j,k} - f_{i-m,j,k}\right). \tag{4}$$

Two finite-difference schemes are available in *Code_Safari*. For high-accurate computations, the optimized 11-point centered finite-difference scheme proposed by Bogey and Bailly [10] is used. This non-dissipative scheme is optimized in the wavenumber space to reduce the dispersion error following the idea of Tam and Webb [9]. In this case, the dispersion error is provided by the difference between the effective wavenumber k^* of the scheme and the exact one in the Fourier space. These two wavenumbers are plotted in Fig. 1a. Only four points per wavelength are required

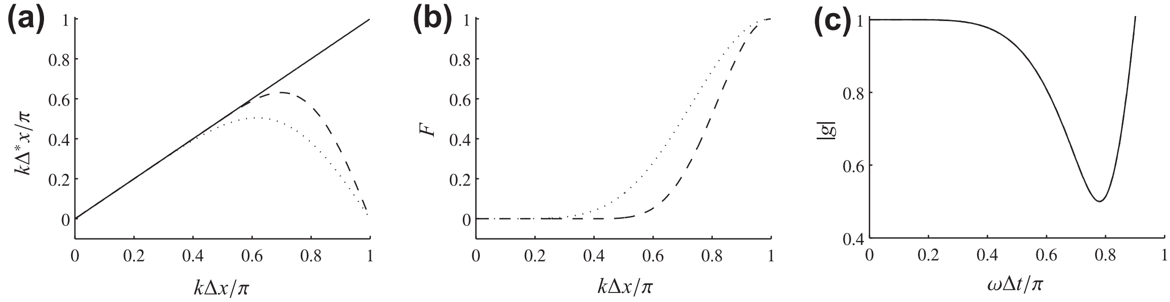

Fig. 1. (a) Effective wavenumber k^* of the spatial discretization versus exact wavenumber k: — spectral, – – – 11-point, ··· 7-point; (b) damping function of the selective filter F versus exact wavenumber k: – – – 11-point, ··· 7-point; (c) dissipative characteristic of the RK4 scheme given by the modulus of the amplification factor $|g|$ versus the angular pulsation ω.

for the resolution of linear waves with the 11-point FD approximation. The same scheme has been applied successfully [21,22] for the simulation of jet noise using LES. For computations around complex geometries, due to cost and robustness constraints, a smaller stencil is used. The standard 7-point centered finite-difference scheme is usually retained. The effective wavenumber of the 7-point FD scheme is also plotted in Fig. 1a showing the higher resolution of the 11-point method. Coefficients s_m of these two schemes are given in Appendix A.

3.2. Temporal integration

The spatial discretization step leads to a semi-discrete form as:

$$\frac{\mathrm{d}\widehat{\boldsymbol{U}}_{i,j,k}}{\mathrm{d}t} + \boldsymbol{R}_{i,j,k} = \boldsymbol{0} \tag{5}$$

with $\boldsymbol{R}_{i,j,k}$ the residual of the discretized inviscid and viscous terms. In the present work, the equations are integrated in time with the classical explicit four-stage Runge–Kutta scheme (RK4):

$$\widehat{\boldsymbol{U}}^{(l)}_{i,j,k} = \widehat{\boldsymbol{U}}^{n}_{i,j,k} - \Delta t \beta^{(l)} \boldsymbol{R}^{(l-1)}_{i,j,k} \quad \forall l \in \{1,\ldots,4\} \tag{6}$$

with $\widehat{\boldsymbol{U}}^{(0)} = \widehat{\boldsymbol{U}}^{n}$. The damping and stability properties of the RK4 scheme are given by the modulus of the amplification factor $|g|$ of the scheme which is shown in Fig. 1c. The coefficients $\beta^{(l)}$ are given in Appendix A. The time step Δt is limited by explicit stability requirement linked to the CFL value defined as CFL = max (CFL$_\xi$,CFL$_\eta$,CFL$_\zeta$) with CFL$_\xi$ = $\max_{i,j,k}(|\lambda^\xi|_{i,j,k}\Delta t/\Delta\xi)$ with $|\lambda^\xi| = |\Theta_\xi| + c\|\nabla\xi\|$ and $c = \sqrt{\gamma p/\rho}$ the speed of sound. Optimized Runge–Kutta schemes can also be used [23].

$$\begin{cases} R_i(u) = \frac{a}{\Delta x}\sum_{m=1}^{N} s_m(u_{i+m} - u_{i-m}) & \text{(spatial discretization)} \\ u_i^{(l)} = u_i^n - \Delta t\beta^{(l)} R_i(u^{(l-1)}) & \forall l \in \{1,\ldots,4\} \text{ (time discretization)} \\ u_i^{n+1} = u_i^{(4)} - \sigma_f\left[d_0 u_i^{(4)} + \sum_{m=1}^{N} d_m\left(u_{i+m}^{(4)} + u_{i-m}^{(4)}\right)\right] & \text{(low-pass filter)} \end{cases}$$

3.3. Low-pass filter

After the application of the Runge–Kutta scheme, the explicit N-point spatial low-pass filter is used to remove spurious high-frequency spatial oscillations:

$$\boldsymbol{W}^{(5)}_{i,j,k} = \boldsymbol{W}^{(4)}_{i,j,k} - \sigma_f\left[\mathcal{L}^\xi_N\left(\boldsymbol{W}^{(4)}_{i,j,k}\right) + \mathcal{L}^\eta_N\left(\boldsymbol{W}^{(4)}_{i,j,k}\right) + \mathcal{L}^\zeta_N\left(\boldsymbol{W}^{(4)}_{i,j,k}\right)\right] \tag{7}$$

where

$$\mathcal{L}^\xi_N(f_{i,j,k}) = d_0 f_{i,j,k} + \sum_{m=1}^{N} d_m(f_{i+m,j,k} + f_{i-m,j,k})$$

with $0 \leqslant \sigma_f \leqslant 1$ the filtering strength; and $\boldsymbol{W} = (\rho, \rho\boldsymbol{u}, p)^T$.

For high-accurate computations, the optimized 11-point filter proposed by Bogey and Bailly [10] is retained. This filter is also optimized in the wavenumber space. The dissipation property of the spatial low-pass filter is given by its damping function F plotted in Fig. 1b corresponding to the Fourier transform of the operator $\mathcal{L}^\xi_N$. The 11-point filter only damps the perturbations not accurately resolved by the spatial scheme presented in Eq. (4). In the same way as before, for computations around complex geometries, the standard 7-point centered low-pass filter is used. The damping function of the 7-point filter is also plotted in Fig. 1b showing the lower dissipation of the 11-point filter. Coefficients d_m of these two filters are given in Appendix A.

3.4. Linear analysis of the discretization errors

The von Neumann method is used to analyze the damping and dispersive properties of the algorithm presented previously. This analysis is only applied on linear equations with periodic boundary conditions. For non-linear equations, the results obtained with the linear analysis are not sufficient. However, linear stability is a necessary condition for non-linear problems [24].

The von Neumann method is applied to the global algorithm (spatial, temporal discretizations and low-pass filter) for the following model linear equation $\partial_t u + a\partial_x u = 0$. The algorithm can be decomposed into three steps as:

with $u_i^{(0)} = u_i^n$.

The von Neumann method is based on the Fourier transform. A single harmonic $u_i^n = \hat{u}^n e^{Iik\Delta x}$ is considered with $\hat{u}^n$ the amplitude, $k\Delta x$ the phase angle corresponding to the wavenumber k and $I^2 = -1$. In order to evaluate the algorithm amplification factor defined as $g = \hat{u}^{n+1}/\hat{u}^n$, the Fourier transform is applied to the three stages of the computation:

$$\begin{cases} \widehat{R}(u) = I\frac{a}{\Delta x}\hat{u}k^{*}\Delta x & \text{with} \quad k^{*}\Delta x = 2\sum_{m=1}^{N} s_m \sin(mk\Delta x)(\text{spatial discret.}) \\ \hat{u}^{(4)} = \left(1+\sum_{l=1}^{4}\gamma_l(-\Delta t I\frac{a}{\Delta x}k^{*}\Delta x)^l\right)\hat{u}^n & \text{with} \quad \gamma_l = \prod_{q=4-l+1}^{4}\beta^{(q)} \quad (\text{time discret.}) \\ \hat{u}^{n+1} = (1-\sigma_f\widehat{D})\hat{u}^{(4)} & \text{with} \quad \widehat{D} = d_0 + 2\sum_{m=1}^{N} d_m\cos(mk\Delta x) \quad (\text{low-pass filter}) \end{cases}$$

Finally, the amplification factor of the global algorithm can be written as:

$$g = (1-\sigma_f\widehat{D})\left(1+\sum_{l=1}^{4}\gamma_l(-I\mathcal{C}_a k^{*}\Delta x)^l\right) \tag{8}$$

with the Courant number $\mathcal{C}_a = \frac{a\Delta t}{\Delta x}(=\mathrm{CFL})$.

The amplification factor g which can be rewritten as $g = |g|e^{I\phi}$ is now compared with the exact factor: $g_{\mathrm{ex}} = e^{-I\mathcal{C}_a k\Delta x}$. The algorithm damping property is given by the norm $|g|$ and the dispersive one by the evolution of the relative phase error: $(\phi + \mathcal{C}_a k\Delta x)/\pi$. The results with CFL = 1 and $\sigma_f = 0.2$ are displayed in Fig. 2. With respect to the damping character of the spatial scheme and the linear filter presented in Fig. 1, by taking CFL = 1, the explicit time integration damages the upper bound of the well-resolved wavenumber range: $k\Delta x \leqslant \pi/2$. To known quantitatively the accuracy domain of the global algorithm, the ratio $\mathcal{H} = g/g_{\mathrm{ex}}$ between the numerical amplification factor and the analytical one is compared to unity using the following arbitrary criterion:

$$|1-\mathcal{H}|\mathrm{LES}5\times 10^{-4} \tag{9}$$

The accuracy domain of the global algorithm is thus reduced to $0 \leqslant k\Delta x \leqslant 0.65$, or equivalently $\lambda_a/\Delta x \approx 9.66$ in term of number of points per wavelength.

3.5. LES approach based on relaxation filtering

The present LES strategy is based on relaxation filtering (LES-RF) detailed in [25]. No structural modeling for the subgrid scale stress tensor is here considered. A functional modeling of the subgrid dissipation is provided by the use of the selective filter in Eq. (7) also employed to remove grid-to-grid oscillations not resolved by centered schemes. Applying directly the filtering operator on the variables ρ, $\rho\boldsymbol{u}$ and p adds, in practice, terms into the flow equations leading to a compressible formalism similar to the one of Vreman [26]. LES-RF has already been investigated and performed in multiple applications [21,22,27–30]. Recently, the influence of the filter shape has been investigated on compressible LES-RF for a low-subsonic high-Reynolds number mixing layer [31]. It has been shown that, on this test case, LES data are sensitive to the effective LES cut-off wavenumber rather than to the filter shape. Thus, with mesh sizes chosen to obtain the same effective LES cut-off wavenumber, numerical results obtained with different numerical filters are similar.

3.6. Shock-capturing procedure

3.6.1. Adaptive shock-capturing filter

A shock-capturing filter is applied on the conservative variables after the use of the selective filter presented in Eq. (7). As proposed by Yee et al. [32], the application of the dissipative part of the shock-capturing procedure is applied after the time integration process as a non-linear filter:

$$\mathrm{U}_{i,j,k}^{n+1} = \mathrm{U}_{i,j,k}^{(5)} + \left(\mathrm{D}_{i,j,k}^{\xi} + \mathrm{D}_{i,j,k}^{\eta} + \mathrm{D}_{i,j,k}^{\zeta}\right), \tag{10}$$

where the dissipative part in the ξ-direction can be expressed as:

$$\mathrm{D}_{i,j,k}^{\xi} = \beta_{i,j,k}^{\xi}(\boldsymbol{\mathcal{D}}_{i+1/2} - \boldsymbol{\mathcal{D}}_{i-1/2}),$$

where $\boldsymbol{\mathcal{D}}_{i+1/2}$ is the dissipative numerical flux of the filtering operator. In *Code_Safari* two different non-linear filters are available and described in the following.

3.6.2. Kim and Lee model

The first filter is based on the artificial dissipation model proposed by Kim and Lee [33]. The same model has been recently used in [34] for shocked nozzles and supersonic diffusers. However, in the present work, only the low-order shock-capturing term of the model of Kim and Lee is applied:

$$\boldsymbol{\mathcal{D}}_{i+1/2} = \frac{\Delta|\lambda|_{i+1/2}^{\xi}}{J_{i+1/2}}\epsilon_{i+1/2}^{(2)}\left(\mathrm{U}_{i+1,j,k}^{(5)} - \mathrm{U}_{i,j,k}^{(5)}\right) \quad \text{and} \quad \beta_{i,j,k}^{\xi} = J_{i,j,k}\frac{\Delta t}{\Delta\xi}. \tag{11}$$

The stencil eigenvalue $\Delta|\lambda|_{i+1/2}^{\xi}$ is defined as:

$$\Delta|\lambda|_{i+1/2}^{\xi} = \max_{m=-2}^{3}(|\lambda^{\xi}|_{i+m,j,k}) - \min_{m=-2}^{3}(|\lambda^{\xi}|_{i+m,j,k}),$$

where the eigenvalue is expressed in the generalized coordinates: $|\lambda^{\xi}| = |\Theta_{\xi}| + c\|\nabla\xi\|$ with $c = \sqrt{\frac{\gamma p}{\rho}}$ the sound speed.

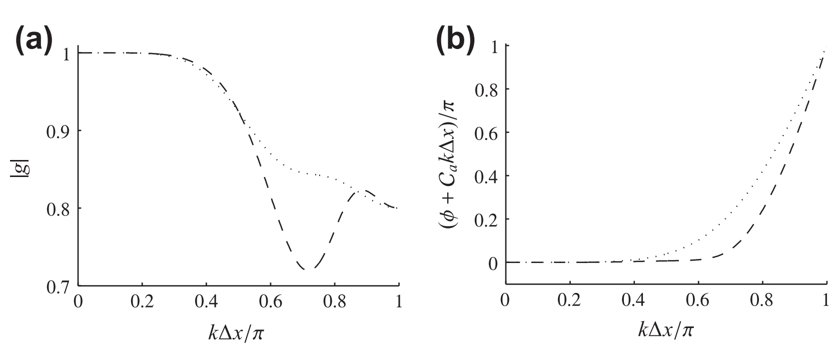

Fig. 2. Damping and dispersion errors as a function of the wavenumber $k\Delta x$: (a) norm of the amplification factor $|g|$; (b) relative phase error $(\phi + \mathcal{C}_a k\Delta x)/\pi$: – – – 11-point, ··· 7-point.

The midpoint value of the transformation Jacobian is estimated by $J_{i+1/2} = (J_i + J_{i+1})/2$. Then, the non-linear dissipation function is expressed:

$$\epsilon^{(2)}_{i+1/2} = \kappa \max_{m=-2}^{3}(\nu^{\xi}_{i+m,j,k}) \quad \text{with} \quad \nu^{\xi}_{i,j,k} = \frac{|p_{i-1,j,k} - 2p_{i,j,k} + p_{i+1,j,k}|}{p_{i-1,j,k} + 2p_{i,j,k} + p_{i+1,j,k}}$$

In this expression ν^{ξ} is the pressure shock detector proposed by Jameson et al. [35]. Finally, the definition of the adaptive control constant κ proposed by Kim and Lee [33] is preserved:

$$\kappa = \frac{1}{\sigma^{1/\alpha}}\left(\frac{\alpha+1}{\alpha-1}\tanh(\alpha-1)\right)^{1+\tanh(\sigma-1)} \quad \text{with}$$
$$\alpha = \frac{|\lambda^{\xi}|^{\max}}{|\lambda^{\xi}|^{\min}} \quad \text{and} \quad \sigma = \frac{p^{\max}}{p^{\min}}$$

where $f^{\max} = \underset{i,j,k}{max} f_{i,j,k}$ and $f^{\min} = \underset{i,j,k}{min} f_{i,j,k}$. The adaptive constant κ makes it possible to control the dissipation strength of the procedure.

According to Garnier et al. [36], the classical high-order shock-capturing schemes show excessive numerical dissipation in the frame of freely decaying turbulence. Thus, a local application of the shock-capturing scheme is necessary to reduce the numerical dissipation, and the determination of the shock location is a crucial problem to minimize this excessive damping. In the filter presented here, this determination is performed via the Jameson sensor. However, in the frame of shock/turbulence interaction [37], the Jameson sensor is not able to distinguish turbulent fluctuations from strong gradients. Therefore, a modified Jameson sensor is proposed in this paper. The Jameson sensor can be rewritten in the following form:

$$\nu^{\xi}_{i,j,k} = \frac{|\mathcal{L}^{\xi}_2(p_{i,j,k})|}{p_{i,j,k} - \mathcal{L}^{\xi}_2(p_{i,j,k})}$$

where $\mathcal{L}^{\xi}_2$ designates the classical linear second-order filter operator:

$$\mathcal{L}^{\xi}_2(p_{i,j,k}) = -\frac{1}{4}p_{i-1,j,k} + \frac{1}{2}p_{i,j,k} - \frac{1}{4}p_{i+1,j,k}.$$

The modified sensor proposed in this paper is based on the use of the N-point selective filter defined in Eq. (7):

$$\begin{cases} \phi^{\xi}_{i,j,k} = \frac{|\mathcal{L}^{\xi}_N(p_{i,j,k})|}{p_{i,j,k} - \mathcal{L}^{\xi}_N(p_{i,j,k})} \\ \text{with } \mathcal{L}^{\xi}_N(p_{i,j,k}) = d_0 p_{i,j,k} + \sum_{m=1}^{N} d_m (p_{i+m,j,k} + p_{i-m,j,k}) \end{cases} \tag{12}$$

The damping feature of the two detectors is compared in 1-D, using a linear analysis. To do that, a plane wave is considered $p_i = e^{-Iki\Delta x}$ where $k\Delta x$ is the phase angle corresponding to the wavenumber k and $I^2 = -1$. In contrast with the Jameson sensor, the modified sensor does not damage the low wavenumber range (see Fig. 3). However, for the high frequencies, the two detectors behave similarly which ensures the shock-capturing property of the scheme. In addition, theses two detectors can be used without modification in the scheme. Moreover, the computational efficiency of the algorithm is not affected by the use of the modified sensor because $\mathcal{L}^{\xi}_N(p_{i,j,k})$ is computed in the selective filtering process in Eq. (7).

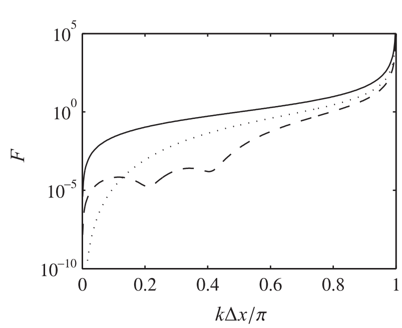

Fig. 3. Damping errors of shock detectors: —- ν^{ξ}_i (classical Jameson sensor), – – – 11-point ϕ^{ξ}_i, ··· 7-point ϕ^{ξ}_i (modified Jameson sensor).

3.6.3. Bogey et al. model

The methodology proposed by Bogey et al. [38] leads to the following dissipative numerical flux:

$$\mathcal{D}_{i+1/2} = \sigma^{sc}_{i+1/2}\sum_{m=1}^{2} c_m (\mathrm{U}_{i+m,j,k} - \mathrm{U}_{i-m+1,j,k}) \quad \text{and} \quad \beta^{\xi}_{i,j,k} = 1 \tag{13}$$

the coefficients c_m are computed via an optimization in the Fourier space. They are given in Appendix A. The adaptive filtering magnitude $\sigma^{sc}_{i+1/2}$ is expressed as:

$$\sigma^{sc}_{i+1/2} = \frac{1}{2}(\sigma^{sc}_i + \sigma^{sc}_{i+1}) \quad \text{with} \quad \sigma^{sc}_i = \frac{1}{2}\left(1 - \frac{r_{th}}{r_i} + \left|1 - \frac{r_{th}}{r_i}\right|\right)$$

r_{th} is a threshold parameter user, as in Visbal and Gaitonde [39] for instance, to specify the regions where the dissipation model is applied. The authors suggest the threshold value $r_{th} = 10^{-4}$. The r_i function is a shock sensor expressed as:

$$r_i = \frac{\mathcal{C}^{\xi}_{i,j,k}}{p^2_{i,j,k}} + \epsilon \quad \text{with} \quad \mathcal{C}^{\xi}_{i,j,k}$$
$$= \frac{1}{2}\left[\left(\mathcal{L}^{\xi}_2(p_{i,j,k}) - \mathcal{L}^{\xi}_2(p_{i+1,j,k})\right)^2 + \left(\mathcal{L}^{\xi}_2(p_{i,j,k}) - \mathcal{L}^{\xi}_2(p_{i-1,j,k})\right)^2\right]$$

and the factor $\epsilon = 10^{-16}$ is used to avoid numerical divergence in the computation of σ^{sc}_i. The authors propose also a shock detection based on dilatation which has been introduced by Ducros et al. [37] for shock/turbulence interaction.

The two dissipation models proposed by Kim and Lee and Bogey et al. are only applied in regions where strong pressure gradients are encountered via their own shock detection. The approach of Kim and Lee is based on the second-order numerical dissipation of the shock-capturing scheme of Jameson et al. [35]. In contrast, the dissipation model of Bogey et al. is based on a second-order numerical filter. These two models are compared in Section 4.

3.6.4. Conservative properties of the algorithm

In order to deal with shock waves, the conservative properties of the spatial scheme are studied in details. As show in Appendix B, N-point FD schemes as the one presented in Eq. (4) can be recasted in a finite-volume framework which ensures conservative properties. In addition, the adaptive non-linear filter in Eq. (10) is conservative due to its finite-volume definition. In Section 4, the shock-capturing ability of the present method is assessed.

3.7. Extension to complex geometries

The high-order finite-difference algorithm satisfying conservation laws in generalized coordinates are limited to curvilinear geometries. In order to go past this limit, overset-grid techniques are used with high-order interpolation procedure to preserve the high-order spatial accuracy [13,15,14]. This is addressed in the following.

3.7.1. Overset-grid strategy

In order to handle complex configurations as those including multiple bodies, the high-order algorithm presented in the previous sections is extended to general overset-grid topologies. In practice, the *Code_Safari* is interfaced with the freely available

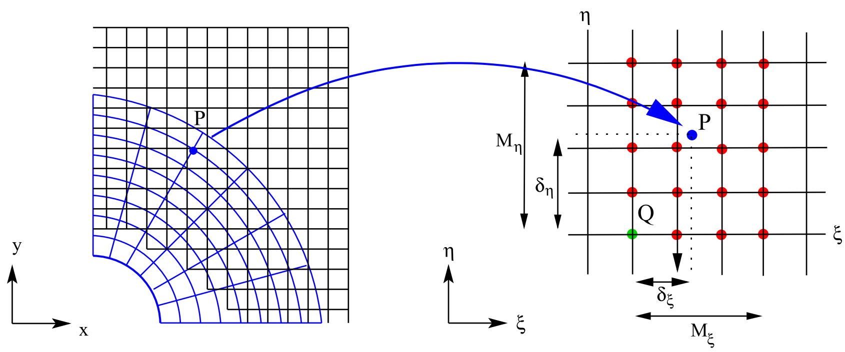

Fig. 4. Example of a 2-D interpolation stencil: 2-D communication between a circular and a Cartesian component grids.

Overture library developed by the Lawrence Livermore National Laboratory [40]. The mesh including different component grids are given by *Overture*. In addition, the interpolation data such as overlapping zones, interpolation stencils and offsets are generated with *Overture*.

3.7.2. High-order interpolation

In the overset-grid approach, points of the different overlapping regions are non coincident. Therefore, the communication between overlapping component grids is performed with high-order interpolation. Sherer and Scott [15] have studied several high accuracy interpolation methods and found that a high-order, explicit Lagrangian method is more accurate and robust. Thus, even DRP interpolation formula have been proposed [41], no DRP properties are involved in the interpolation procedure used here. The interpolation process is performed in the computational domain (ξ,η,ζ) as in Fig. 4. In 2-D, the evaluation of the variable ϕ at the point P is performed via the interpolation of ϕ at P as:

$$\phi_P \approx \sum_{i=0}^{M_\xi-1}\sum_{j=0}^{M_\eta-1} L_i^\xi L_j^\eta \phi_{I_Q+i,J_Q+j}. \tag{14}$$

where M_ξ and M_η are the interpolation stencil length in the ξ- and η-direction respectively. Q is the first donor point of the interpolation stencil (in green[1] in Fig. 4) and its coordinates are (I_Q,J_Q). L_i^ξ and L_j^η are the Lagrangian coefficients in the two directions defined as:

$$L_i^\xi = \prod_{m=0,m\neq i}^{M_\xi-1} \frac{\delta_\xi - m}{i-m} \quad \text{and} \quad L_j^\eta = \prod_{m=0,m\neq j}^{M_\eta-1} \frac{\delta_\eta - m}{j-m}$$

where δ_ξ and δ_η called the offsets are the coordinates of P, the receiver point, with respect to Q in the computational domain. For simplicity and isotropic reason, in the following, we have chosen $M_\xi = M_\eta = N_{\text{order}}$ which is also the Lagrangian polynomial order in the computational domain.

In addition, the *Code_Safari* code is parallelized by domain decomposition on each component grid for application to massively-parallel platforms. The communication between each domain is performed via the MPI library.

3.7.3. Linear analysis of the interpolation errors

In 1-D (cf. Fig. 5), the Lagrangian interpolation procedure in Eq. (14) can be rewritten as follows:

$$\phi(x_P) \approx \sum_{i=0}^{N_{\text{order}}-1} L_i \phi(x_Q + i\Delta x) \quad \text{with} \quad L_i = \prod_{m=0,m\neq i}^{N_{\text{order}}-1} \frac{\delta - m}{i-m} \tag{15}$$

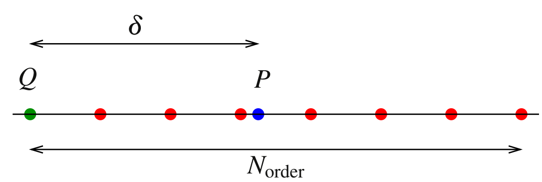

Fig. 5. Example of a 1-D interpolation stencil.

with $x_P = x_Q + \delta\Delta x$. The interpolation error is now quantified using a one-dimensional Fourier error analysis following Sherer and Scott [15]. Thus, a single harmonic is considered: $\phi(x) = e^{Ikx}$ as previously with the wavenumber k and $I^2 = -1$. The interpolation error factor can be defined as:

$$\mathcal{H}_{\text{itp}} = \sum_{i=0}^{N_{\text{order}}-1} L_i e^{Iik\Delta x}/e^{I\delta k\Delta x}$$

For a centered Lagrangian interpolation, we have $\delta \approx (N_{\text{order}}-1)/2$. The local error is displayed in Fig. 6. The Lagrangian interpolation procedure with $N_{\text{order}} = 2$ or $N_{\text{order}} = 4$ implies numerical errors in the wavenumber range not damped by the present algorithm according to the results displayed in Fig. 2. This can lead to the generation of spurious waves. In contrast, Lagrangian interpolation with $N_{\text{order}} = 6$ or $N_{\text{order}} = 8$ seems to be suitable with the present numerical algorithm. To compare quantitatively the different polynomial interpolation, the limit accuracy limit in Eq. (9) is still used: $|1-\mathcal{H}_{\text{itp}}| \leqslant 5\times10^{-4}$. The accuracy domains are given in Table 1. The range of wavenumber well resolved by the present algorithm is thus incorporated in the one of the Lagrangian polynomial interpolation with $N_{\text{order}} = 6$ and $N_{\text{order}} = 8$.

3.8. Boundary conditions

3.8.1. Wall boundaries

In order to preserve low-dissipation and low-dispersion properties near the wall boundaries, non-centered finite-difference schemes in conjunction with explicit non-centered low-pass filter are used. For example, when the 11-point algorithm is used, the finite-difference schemes and the linear filters proposed by Berland et al. [42] are retained. These two spatial operators are optimized in the wavenumber space to recover the bandwidth properties of the centered ones presented in Eqs. (4) and (7). However, the non-centered schemes suffer from numerical stability. Therefore, in the case of strong flow gradients near wall boundaries, explicit centered filtering of lower order can be used optionally to ensure the numerical stability.

In the following a wall boundary denoted Γ at $\eta = \text{cst}$ is considered.

[1] For interpretation of color in Figs. 4, 5, 11, 15, 19, 20, 22, and 23, the reader is referred to the web version of this article.

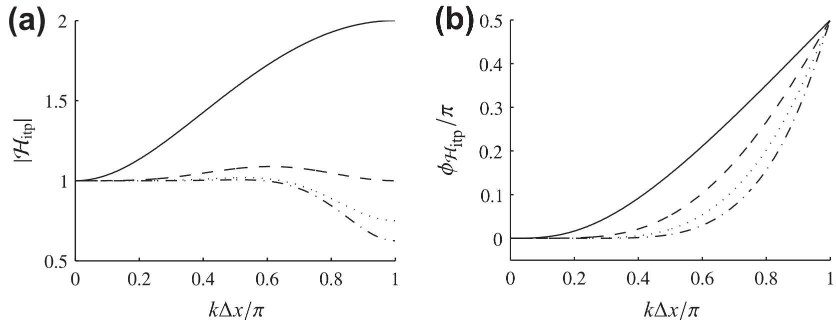

Fig. 6. Local error of the interpolation process with — $N_{\rm order}$ = 2, – – – $N_{\rm order}$ = 4, ⋯ $N_{\rm order}$ = 6 and –·–·– $N_{\rm order}$ = 8: (a) dissipation and (b) dispersion errors.

Table 1
Accuracy limit of the Lagrangian interpolations with $N_{\rm order}$ = 2,4,6 and 8.

$N_{\rm order}$	2	4	6	8
$k_a\Delta x$	0.04	0.34	0.65	0.90
$\lambda_a/\Delta x$	169.81	18.48	9.59	6.94

Inviscid flow. For an inviscid flow, the wall conditions are:

$$\Theta_\eta = 0,\quad \partial_\xi\Theta_\eta = 0,\quad \partial_\zeta\Theta_\eta = 0 \quad \text{and} \quad \frac{\mathrm{d}}{\mathrm{d}t}\Theta_\eta = 0 \quad \text{on } \Gamma \tag{16}$$

Thus on the wall Γ:

$$\mathsf{F}_\eta|_\Gamma = \frac{1}{J}\begin{pmatrix}0\\ p\nabla\eta\\ 0\end{pmatrix} \quad \text{and} \quad \partial_t\Theta_\eta|_\Gamma = 0$$

To obtain the wall pressure $p|_\Gamma$, the momentum equation is considered:

$$\partial_t\left(\frac{1}{J}\rho\mathsf{u}\right) + \partial_\xi\left(\frac{1}{J}[\rho\mathsf{u}\Theta_\xi + p\nabla\xi]\right) + \partial_\eta\left(\frac{1}{J}[\rho\mathsf{u}\Theta_\eta + p\nabla\eta]\right) + \partial_\zeta\left(\frac{1}{J}[\rho\mathsf{u}\Theta_\zeta + p\nabla\zeta]\right) = \mathbf{0}$$

with the use of the continuity equation and Eq. (2):

$$\underbrace{\frac{1}{J}\rho\left(\partial_t\mathsf{u} + \Theta_\xi\partial_\xi\mathsf{u} + \Theta_\eta\partial_\eta\mathsf{u} + \Theta_\zeta\partial_\zeta\mathsf{u}\right)}_{=\frac{1}{J}\rho\frac{\mathrm{d}\mathsf{u}}{\mathrm{d}t}} + \underbrace{\partial_\xi\left(\frac{1}{J}p\nabla\xi\right) + \partial_\eta\left(\frac{1}{J}p\nabla\eta\right) + \partial_\zeta\left(\frac{1}{J}p\nabla\zeta\right)}_{=\frac{1}{J}(\nabla\xi\partial_\xi p + \nabla\eta\partial_\eta p + \nabla\zeta\partial_\zeta p)} = \mathbf{0}$$

The projection following the vector $\nabla\eta$ on the wall Γ leads to:

$$-\rho\mathsf{u}\cdot\frac{\mathrm{d}\nabla\eta}{\mathrm{d}t} + (\nabla\xi\partial_\xi p + \nabla\eta\partial_\eta p + \nabla\zeta\partial_\zeta p)\cdot\nabla\eta = 0$$

As the mesh is fixed ($\partial_t\nabla\eta = \mathbf{0}$) and $\Theta_\eta|_\Gamma = 0$, it can be written as follows:

$$-\rho\mathsf{u}\cdot(\Theta_\xi\partial_\xi\nabla\eta + \Theta_\zeta\partial_\zeta\nabla\eta) + \partial_\xi p(\nabla\xi\cdot\nabla\eta) + \partial_\eta p\|\nabla\eta\|^2 + \partial_\zeta p(\nabla\zeta\cdot\nabla\eta) = 0$$

Using Eq. (16) the projection of the momentum equation is:

$$\rho\nabla\eta\cdot(\Theta_\xi\partial_\xi\mathsf{u} + \Theta_\zeta\partial_\zeta\mathsf{u}) + \partial_\xi p(\nabla\xi\cdot\nabla\eta) + \partial_\eta p\|\nabla\eta\|^2 + \partial_\zeta p(\nabla\zeta\cdot\nabla\eta) = 0$$

Finally, the derivative of the pressure is given by:

$$\partial_\eta p|_\Gamma = -\frac{1}{\|\nabla\eta\|^2}[\partial_\xi p(\nabla\xi\cdot\nabla\eta) + \partial_\zeta p(\nabla\zeta\cdot\nabla\eta) + \rho\nabla\eta\cdot(\Theta_\xi\partial_\xi\mathsf{u} + \Theta_\zeta\partial_\zeta\mathsf{u})] \tag{17}$$

Viscous flow. For a viscous flow, the adiabatic wall conditions are:

$$\mathsf{u} = \mathbf{0},\quad \partial_\xi\mathsf{u} = \mathbf{0},\quad \partial_\zeta\mathsf{u} = \mathbf{0},\quad \frac{\mathrm{d}}{\mathrm{d}t}\mathsf{u} = \mathbf{0} \quad \text{and} \quad \mathsf{q}\cdot\nabla\eta = 0 \quad \text{on} \quad \Gamma \tag{18}$$

Thus on the wall Γ, the inviscid fluxes are:

$$\mathsf{F}_\xi|_\Gamma = \frac{1}{J}\begin{pmatrix}0\\ p\nabla\xi\\ 0\end{pmatrix},\quad \mathsf{F}_\eta|_\Gamma = \frac{1}{J}\begin{pmatrix}0\\ p\nabla\eta\\ 0\end{pmatrix},\quad \mathsf{F}_\zeta|_\Gamma = \frac{1}{J}\begin{pmatrix}0\\ p\nabla\zeta\\ 0\end{pmatrix}.$$

and the viscous fluxes

$$\mathsf{F}^v_\xi|_\Gamma = \frac{1}{J}\begin{pmatrix}0\\ \mathcal{V}_\xi\\ -\mathsf{q}\cdot\nabla\xi\end{pmatrix},\quad \mathsf{F}^v_\eta|_\Gamma = \frac{1}{J}\begin{pmatrix}0\\ \mathcal{V}_\eta\\ 0\end{pmatrix},\quad \mathsf{F}^v_\zeta|_\Gamma = \frac{1}{J}\begin{pmatrix}0\\ \mathcal{V}_\zeta\\ -\mathsf{q}\cdot\nabla\zeta\end{pmatrix}.$$

In the same way as for the inviscid flow, the momentum equation is projected following the vector $\nabla\eta$ on the wall Γ. With neglecting viscous terms in this equation, this leads to the following derivative of the pressure:

$$\partial_\eta p|_\Gamma = -\frac{1}{\|\nabla\eta\|^2}[\partial_\xi p(\nabla\xi\cdot\nabla\eta) + \partial_\zeta p(\nabla\zeta\cdot\nabla\eta)] \tag{19}$$

The value of the wall pressure is approximated as follows:

$$p_{i,0,k} = p_{i,1,k} + \partial_\eta p|_\Gamma\Delta\eta$$

with the spatial derivative given by Eq. (17) or (19).

3.8.2. Non-reflective boundary conditions

Inlet and outlet boundary conditions are based on the Thompson's characteristic boundary conditions [43]. The conditions are supposed to be locally one dimensional and inviscid. Then, the convective terms in the boundary-normal direction are split into several waves with different characteristic velocities. Finally, the unknown incoming waves are expressed in function of known outgoing waves. The 3-D far-field radiation boundary conditions generalized by Bogey and Bailly [44] are applied on the boundaries where only acoustic perturbations are present.

4. Numerical examples

In this section, several canonical problems are reported. These cases involve classical problems encountered in Computational AeroAcoustics (CAA) as well as in computational fluid dynamics (CFD).

The conservative and shock-capturing properties of the proposed algorithm are evaluated on classical 1-D shock tube and

2-D inviscid flow with discontinuities. The interaction shock/vortex is also retained to check that the non-linear shock-capturing procedure does not damage the bandwidth properties of the spatial discretization.

In addition, the use of overlapping regions can generate spurious acoustic waves as it has been observed by Desquesnes et al. [14]. In the present paper, the influence of the polynomial order on the accuracy of the finite-difference scheme and on the generation of spurious acoustic waves is characterized. Two numerical test cases are retained: the convection of an inviscid vortex through overset regions and the diffraction of a monopolar acoustic source by a cylinder. Finally, the realistic rod-airfoil configuration including multiple solid bodies and characterized by multiple physical scales is studied via LES.

Table 2 sums up the different properties of the proposed algorithm validated by the present test cases.

Table 2
Review of the different numerical properties of the present algorithm and the test cases associated.

Test cases	Propagation	Shock-capturing	Overset	Wall	Steady
1: Sod mono		×			×
2: M3 step		×		×	×
3: SVI	×	×			
4: Vortex	×		×		
5: Sod multi		×	×		×
6: Diffraction	×		×	×	
7: Rod-airfoil	×		×	×	

In this section, all test cases are carried out with the 11-point FD scheme unless it is mentioned that the 7-point FD scheme is used.

4.1. Sod's shock tube problem

First, the classical 1-D Sod's shock tube is considered. It is solved using the 1-D Euler equations and the initial conditions are $(\rho,u,p) = (1,0,0)$ for $x < 0$ and $(\rho,u,p) = (0.125,0,0.1)$ otherwise. Results are displayed in Fig. 7 with CFL = 0.5 and $\sigma_f = 0.2$. Only 100 cells ($\Delta x = 1/100$) are used for the computational domain $[-0.5;0.5]$ as in Jiang and Shu [6]. The numerical solutions obtained with the Kim and Lee and the Bogey et al. dissipation model are compared with the exact solution. The 3-shock wave is very well represented with a minimum of diffusion. The 2-contact discontinuity is well located by the algorithm with a diffusive character. Only the end of the 1-rarefaction wave is not well located. On the pressure variable, some classical Gibbs oscillations are observed upstream the position of the shock wave. The dissipation model proposed by Bogey et al. seems to be a little more dissipative than the one of Kim and Lee. This is visible in the shock profile and in the damping of the Gibbs oscillations. Thus, in the following, only the dissipative flux of Kim and Lee are used for the shock-capturing abilities.

4.2. Two-dimensional Mach 3 wind tunnel with a step

The second well-known test case is the Mach 3 wind tunnel with a step studied by Woodward and Colella [45]. The problem is initialized with a 2-D inviscid Mach 3 flow in the wind tunnel.

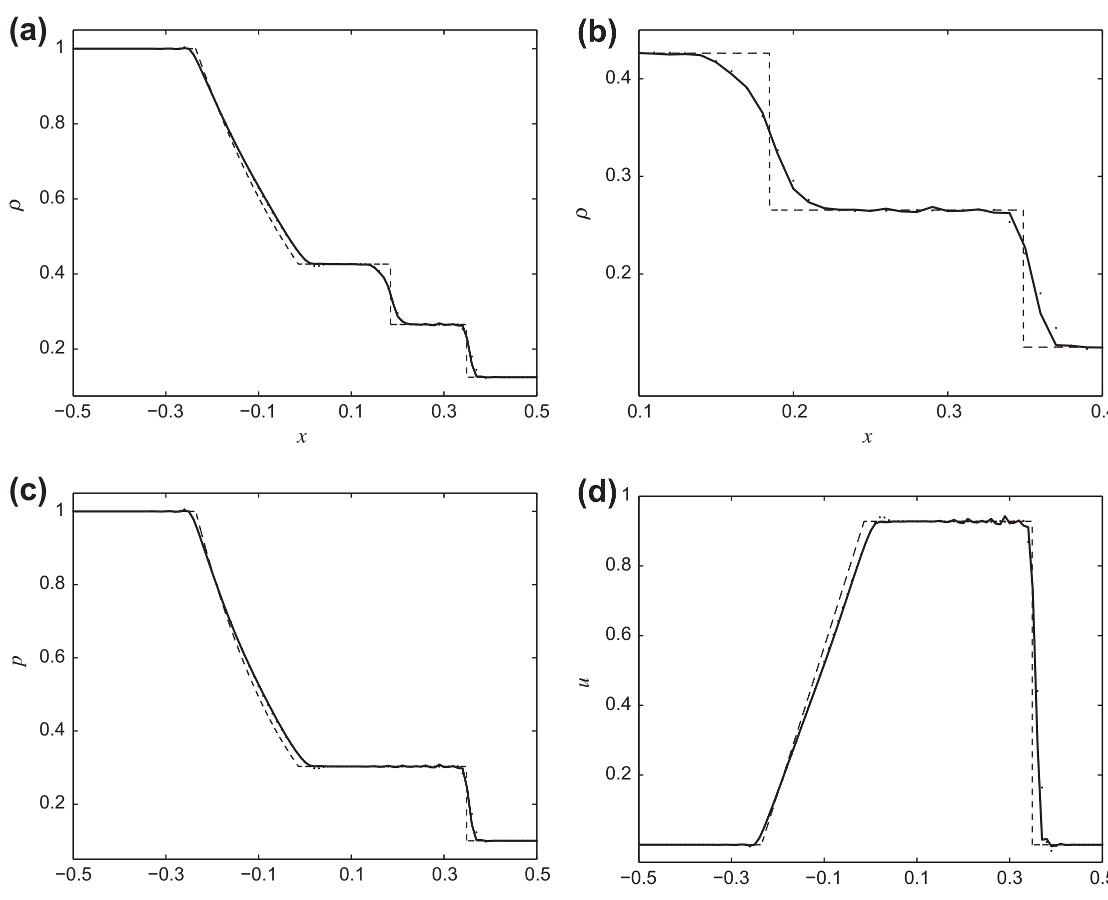

Fig. 7. Comparison between analytical and numerical solutions for the Sod's shock tube with 100 cells: (a) density; (b) zoom density variable ; (c) pressure; (d) velocity: – – – exact solution, — Kim and Lee model, ··· Bogey et al. model.

Reflective boundary conditions are applied along the walls, whereas the inflow and outflow conditions are applied via the characteristics. No specific treatment is used for the singularity at the corner of the step. The grid resolution is the same as the one used by Woodward and Colella [45] and by Jiang and Shu [6]: $N_\xi \times N_\eta = 241 \times 81$ grid points. Density contours with CFL = 0.2 and $\sigma_f = 0.2$ are represented in Fig. 8 and compared to the numerical solution obtained by Jiang and Shu [6] with a fifth-order WENO scheme. The flow exhibits multiple shock reflections and interactions between different types of discontinuity. The positions of shocks are accurately represented. Kelvin–Helmholtz oscillations generated at the triple point are clearly visible. The resolution of the 7-point FD scheme with the Kim and Lee model is similar to the one of the WENO-5 scheme. The higher resolution obtained with the 11-point scheme is shown by the presence of small classical Gibbs oscillations.

4.3. Two-dimensional shock/vortex interaction

This test case describes the interaction between a stationary shock and an inviscid vortex [6]. The computational domain is taken to be $[-1,1] \times [-0.5,0.5]$. A stationary Mach 1.1 shock normal to the x-axis is located at $x_s = -0.5$. Its left side is $(\rho, u, v, p)_L = (1, 1.1\sqrt{\gamma}, 0, 1)$ and its right side is obtained with the Rankine-Hugoniot relations. A vortex is superposed to the flow and centers at $(x_c, y_c) = (-0.75, 0)$. According to [6], the vortex is described as a perturbation of the velocity (u,v), the entropy $S = \ln(p/\rho^\gamma)$ and the temperature $T = p/\rho$ of the base flow:

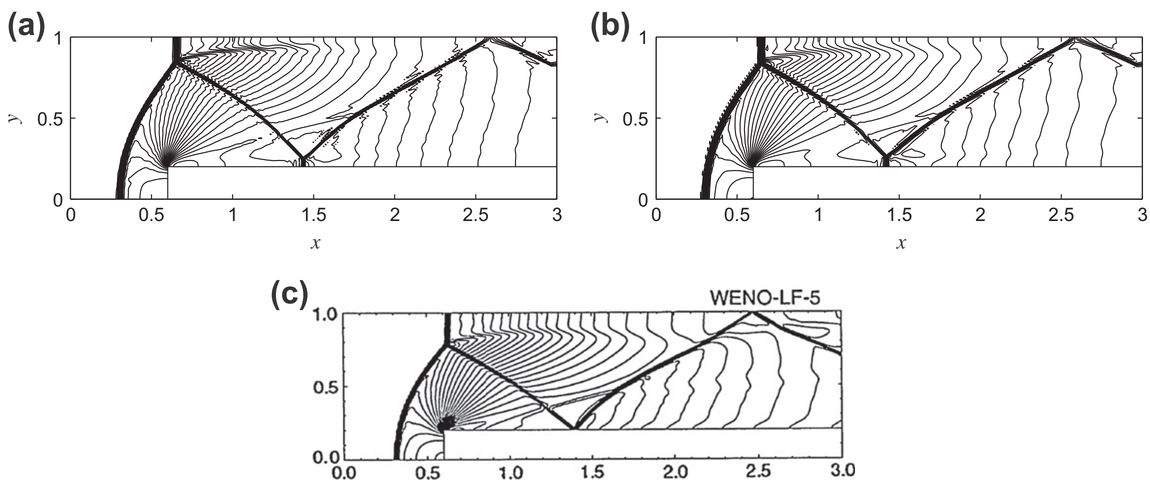

Fig. 8. Inviscid 2-D Mach 3 flow past a step: density contour at $t = 4$: 30 contours from 0.2568 to 6.607. (a) 11-point FD scheme with Kim and Lee model; (b) 7-point FD scheme with Kim and Lee model; (c) numerical solution obtained with WENO-5 scheme [6].

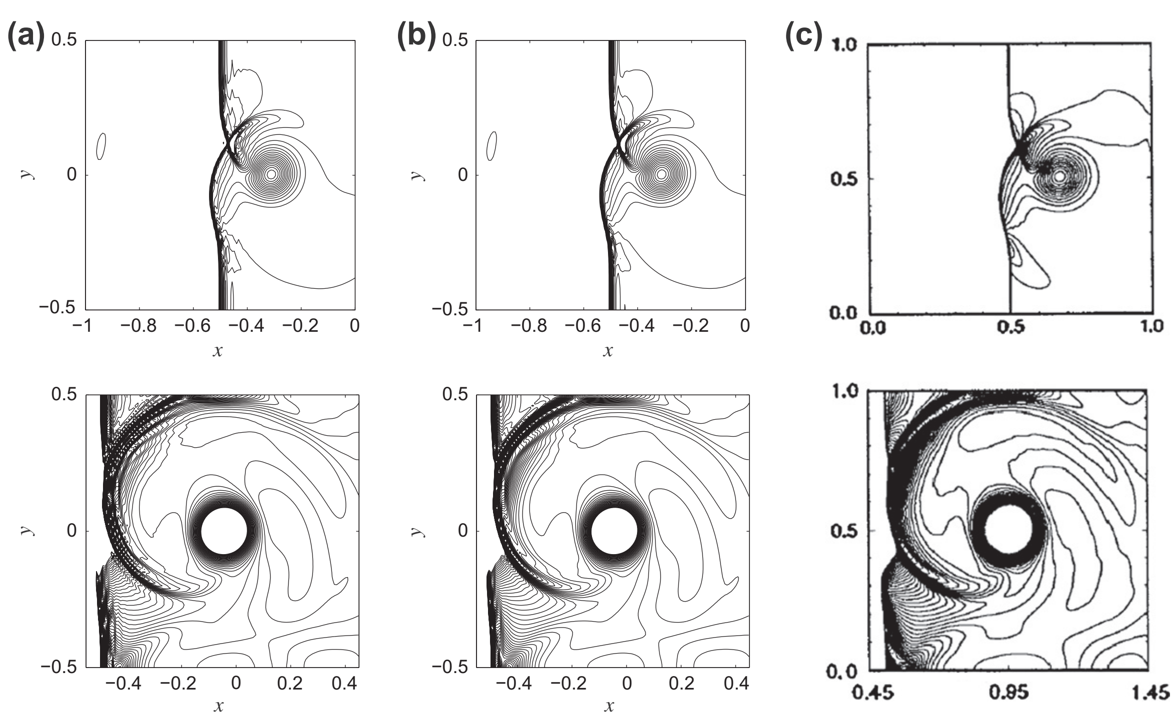

Fig. 9. Inviscid vortex/shock interaction, pressure iso-contours. Top pictures: 30 contours from 1.02 to 1.4 at $t = 0.35$. Bottom pictures: 90 contours from 1.19 to 1.37 at $t = 0.60$. (a) 11-point FD scheme with Kim and Lee model; (b) 7-point FD scheme with Kim and Lee model; (c) WENO-5 scheme [6].

$$\begin{cases} \delta u = \epsilon a e^{\alpha(1-a^2)}(y - y_c)/r \\ \delta v = \epsilon a e^{\alpha(1-a^2)}(x_c - x)/r \\ \delta S = 0 \\ \delta T = (1-\gamma)\epsilon^2 e^{2\alpha(1-a^2)}/4\alpha\gamma \end{cases} \quad \text{with} \quad \begin{cases} a = r/r_c \\ r = \sqrt{(x-x_c)^2 + (y-y_c)^2} \\ r_c = 0.05 \\ \epsilon = 0.3 \\ \alpha = 0.204 \end{cases}$$

The computation is performed with an uniform grid of 251×101 points as used by Jiang and Shu [6] and with CFL = 0.9 and $\sigma_f = 0.2$. The upper and lower boundaries are set to be reflective. The results plotted in Figs. 9 and 10 are in good agreement with the ones obtained by Jiang and Shu [6] with a fifth-order WENO scheme. In particular, the phenomenon of the curved shock at $t = 0.35$, an accurate vortex/shock resolution at $t = 0.60$ and the reflections near the borders at $t = 0.8$ are retrieved. Some Gibbs oscillations are still visible in the FD solutions especially with the 11-point FD method showing its high resolution.

4.4. Two-dimensional advection of a vortex through interpolation zones

The vortex is defined by the initial conditions:

$$\begin{cases} \rho = 1 \\ u = M_\infty + y\epsilon \exp\left(-\frac{\log(2)}{\alpha^2}(x^2+y^2)\right) \\ v = x\epsilon \exp\left(-\frac{\log(2)}{\alpha^2}(x^2+y^2)\right) \\ p = \frac{1}{\gamma} \end{cases}$$

with $M_\infty = 0.5$ the freestream Mach number, $\epsilon = 0.01$ the vortex strength and $\alpha = 3\Delta x$ the Gaussian half width. The computational domain composed by three uniform component grids connected by two overlapping regions, is displayed in Fig. 11a. The left and the right grids contain $N_\xi \times N_\eta = 51 \times 51$ points. The center grid consists of $N_\xi \times N_\eta = 51 \times 52$ points and is shifted by half a grid size length in x-direction such as displayed in Fig. 11b. This avoids interpolation points to coincide with grid points in the zone of the passage of the vortex travel. The radiation boundary conditions are applied to all boundaries. Five simulations are done with varying interpolation order ranging from 2 to 10 with CFL = 0.25 to avoid temporal errors. The simulations are carried out for 800 iterations, the time required to translate the vortex $100\Delta x$ and to ensure the transit through the two overlapping regions.

Fig. 12 displays a sequence of the instantaneous pressure field when the vortex meets the first overlap region using Lagrangian polynomials of order $N_{\text{order}} = 2{,}6$ and 10. The acoustic wave just leaving the computational domain at the first and second instant is due to an adaptation of the pressure field to the velocity field at the beginning of the simulation. Using the second-order interpolation, strong acoustic disturbances are generated and contaminate the solution. Those parasite waves are significantly reduced when using sixth-order Lagrangian polynomials and disappear with a tenth-order interpolation. This non-linear numerical example supports the previous linear analysis.

To quantify the generation of spurious acoustic perturbations, the time evolution of the L_2 norm of the residual pressure in the left grid is studied:

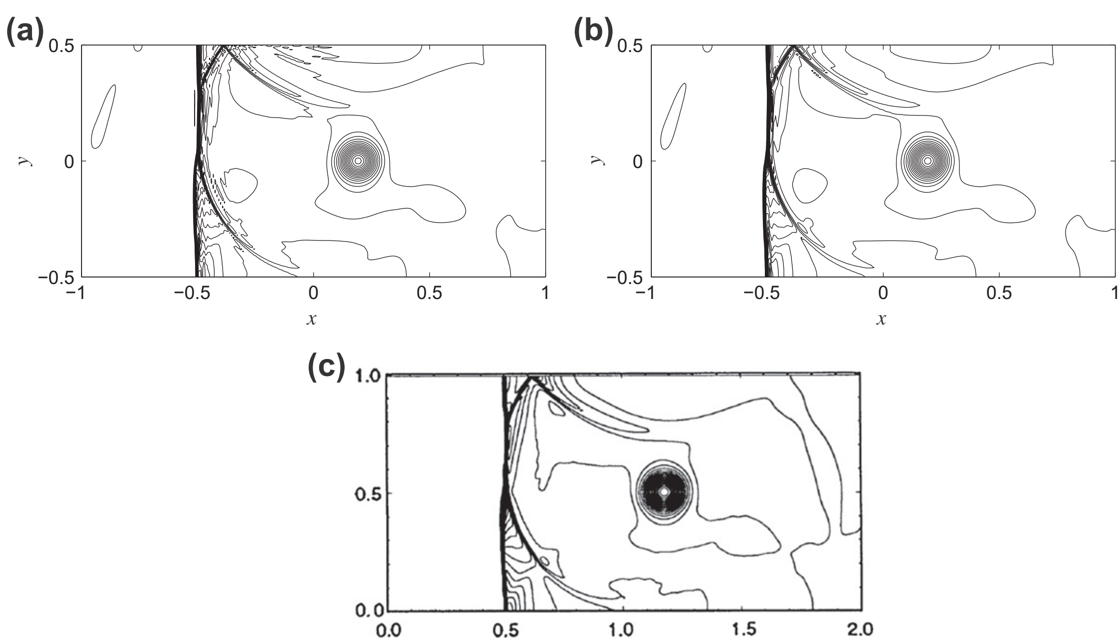

Fig. 10. Inviscid vortex/shock interaction, pressure iso-contours. Thirty contours from 1.02 to 1.4 at $t = 0.80$. (a) 11-Point FD scheme with Kim and Lee model; (b) 7-point FD scheme with Kim and Lee model; (c) WENO-5 scheme [6].

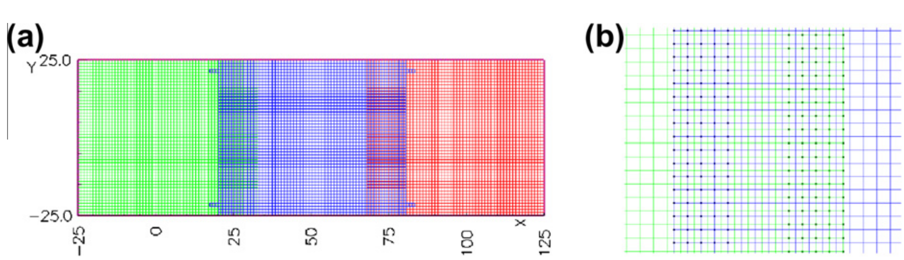

Fig. 11. Overlapping grid: (a) general view; (b) detailed view of the center of an overlapping region ($y = 0$).

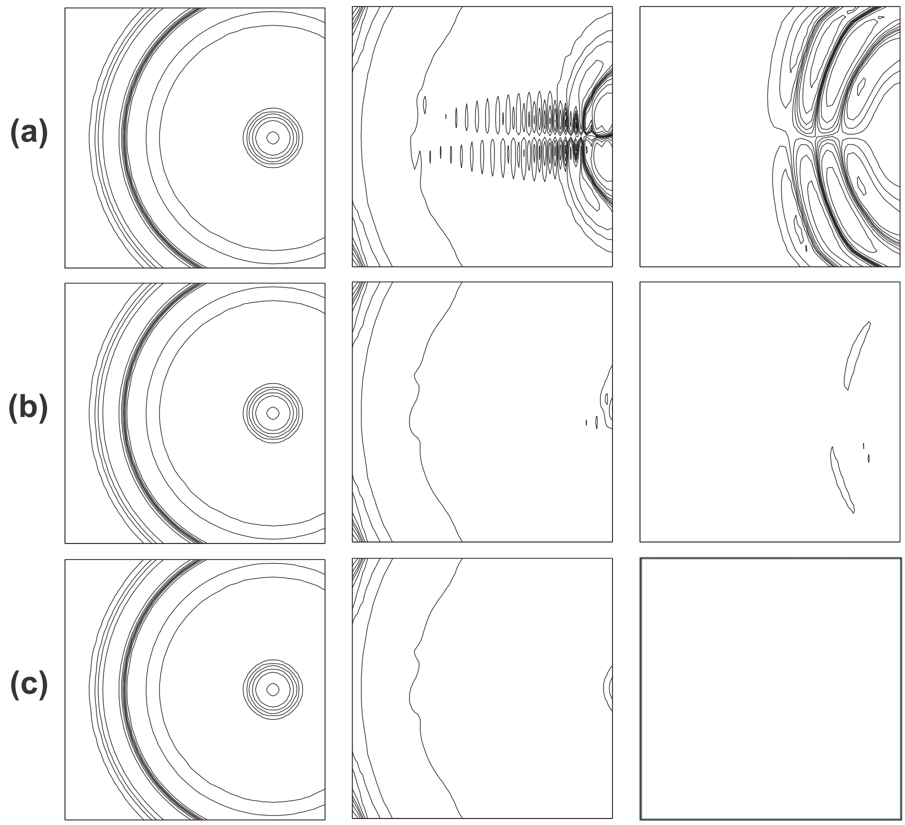

Fig. 12. Iso-contours of the instantaneous pressure field computed in the left grid during the passage of the vortex through the overlapping region using Lagrangian polynomials of order: (a) $N_{\text{order}} = 2$; (b) $N_{\text{order}} = 6$ and (c) $N_{\text{order}} = 10$.

$$R_p = \sqrt{\frac{1}{N_\xi N_\eta}\sum\nolimits_{i,j}^{N_\xi,N_\eta} p'^2_{i,j}}.$$

This residual obtained with the overset-grid approach is compared to the reference single-block computation in Fig. 13. The peak observed during the first 200 iterations for all setups is associated to the transitional pressure pulse. The decrease of the residual pressure, indicates that this pressure pulse leaves the computational domain without any spurious reflections. When the vortex hits the overlapping zone (Nit = 200), the residual pressure obtained with second-order polynomials shows a significant increase and confirms the generation of acoustic waves observed in Fig. 12a. Using fourth-order polynomials the reflections are only visible in a zoom on the last 600 iterations given in Fig. 13b. For orders higher than 6 the residual pressure evolves like in the single block computation and the reflections are negligible.

Finally, to quantify the error on the aerodynamic field, the L_2 norm of the difference between the exact and the computational swirl velocity when the vortex has reached its final position at $x = 100\ \Delta x$ is considered. The error is computed along the x-axis at $y = 0$ such as:

$$L_v = \sqrt{\frac{1}{N_\xi}\sum\nolimits_{i}^{N_\xi} v_i|^2_{y=0}}.$$

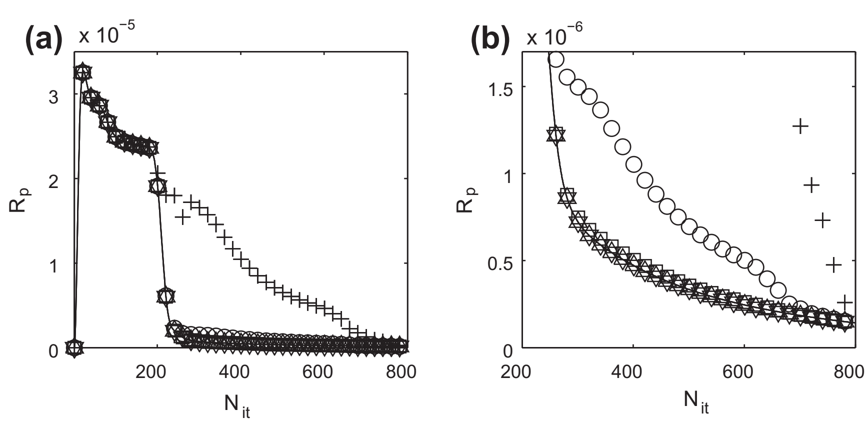

Fig. 13. (a) Time evolution of the residual pressure R_p in the left grid. (b) Detailed view on the residual pressure; — R_p of the single-block computation (reference solution); solution obtained with overset grids using different interpolation orders + $N_{\text{order}} = 2$, ○ $N_{\text{order}} = 4$, □ $N_{\text{order}} = 6$, △ $N_{\text{order}} = 8$, ▽ $N_{\text{order}} = 10$.

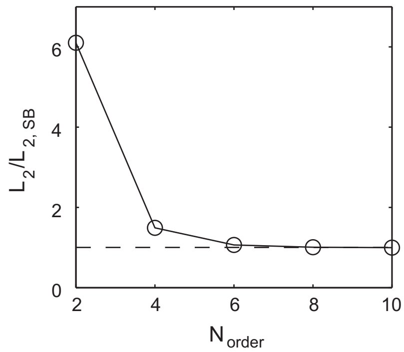

Fig. 14. L_2 norm of the error of the swirl velocity normalized by the L_2 norm obtained for the computation on a single block.

The L_v values normalized by the single-block result are plotted in Fig. 14. It reveals that for polynomial orders higher than 6 the accuracy of the numerical algorithm is only governed by the spatial and temporal errors: the interpolation error becomes negligible. In order to reduce the effort in CPU and storage, the order of interpolation polynomials is limited to eighth-order for 2-D problems and to sixth-order for 3-D problems in the present work. When using the 7-point scheme for complex geometries, the fourth-order interpolation is chosen in the aim of reducing CPU costs and taking into account an accuracy balance between the numerical schemes and the interpolation procedure.

4.5. One-dimensional shock tube with two-dimensional overlapping grids

As the interpolation procedure does not ensure the conservative property of the global algorithm, it is necessary to evaluate the damage caused by this process on the computation by revisiting for instance the Sod's shock tube computed previously on a single block. Consider now the 2-D computational domain: $[-0.5;0.5]\times[-0.25;0.25]$, composed by two Cartesian component grids plotted in Fig. 15. One of the two grids is completely embedded in the other one. The grid size $\Delta x=\Delta y=1/100$ is the same for the two grids and corresponds to the one used in the single-block computation. As in the previous Section, the center grid is shifted by half a grid size in the two directions. In addition, to assess the influence of the interpolation procedure, Lagrangian polynomials of order $N_{order}=2,4,6,8$ and 10 are used. The numerical solutions are seen at $y=-0.15$ in the lower overlapping zone and are compared to the numerical results obtained with only one Cartesian domain. Multi-block solutions with $N_{order}=2$ and $N_{order}=8$ are compared to the single-block solution in Fig. 16. The interpolation procedure slightly modifies the waves speed and generates spurious oscillations. Increasing the order of Lagrangian polynomials damps the magnitude of these oscillations.

4.6. Diffraction of monopolar acoustic source by a cylinder

This test case is issued from the second CAA workshop [46] and serves to check if sixth-order Lagrangian polynomials are sufficient to recover the accuracy of the high-order finite-difference scheme when only acoustic perturbations are involved. The numerical set-up is represented in Fig. 17. The 2-D Euler equations are solved in non-dimensional form. A Gaussian shaped source is placed at $(x_s,y_s)=(4,0)$:

$$S=\epsilon\sin(\omega t)\exp\left[\ln(2)\frac{(x-x_s)^2+(y-y_s)^2}{b^2}\right],$$

where the angular frequency is given by $\omega=8\pi$ and the Gaussian half-width by $b=0.2$. Originally the test case proposes to solve the linearized Euler equations. For the non-linear Euler equations, a sufficiently small source strength ϵ ($\epsilon=1\times10^{-6}$ in the present work) has to be introduced, in order to avoid non-linear effects. For initial conditions air at rest at the pressure $p_0=1/\gamma$ and with the density $\rho_0=1$ is taken. The wave length associated to the source is $\lambda=c_0/4=0.25$. Note that the source is non compact since the wave length is of the same order as the source size.

A first simulation is done using a single cylindrical grid which contains $N_r\times N_\theta=781\times751=5.9\times10^5$ grid points spaced uniformly in r- and θ-direction. The number of points in the azimuthal direction N_θ is chosen to ensure a wave to be resolved by seven points at $r/d=7.5$. The number of points in radial direction N_r is taken to respect a ratio $\Delta r/\Delta\theta=1.5$ at the cylinder wall. The directivity given by:

$$D(\theta,r)=r\frac{1}{T}\int^{T}p'(\theta,r)^2\,\mathrm{d}t$$

is computed on a arc with $r/d=7.5$ and $\pi/2\leqslant\theta\leqslant\pi$ and is compared to the analytical solution of the problem. The computed and analytical curves compare well in Fig. 18 showing a good agreement.

Fig. 19a shows the simulated fluctuating pressure field. The acoustic waves coming from the non-compact source generate a diffraction field. A silent zone behind the cylinder can be observed.

In a second simulation the same test case will be done using the overset-grid approach. The overset grid is composed of two grids: one cylindrical grid and one uniform grid. The uniform one is generated to resolve acoustic wave with seven points per wave length $\Delta x=\Delta y=\lambda/7=1/28$ and is extended $-10\leqslant x,y\leqslant10$. The cylindrical grid is spaced uniformly in azimuthal and radial direction and is limited by the outer radius $r_a/d=1.5$. In the radial direction the grid length is chosen to be $\lambda/13$ and the number of grid points in azimuthal direction is taken to ensure that the aspect ratio of the

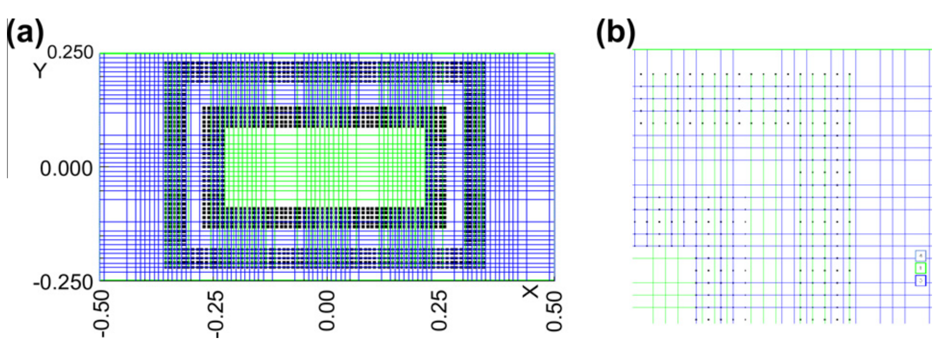

Fig. 15. Computation of the Sod's shock-tube with overlapping grids: (a) general view of the computational domain with the two grids; (b) detailed view of the overlapping region.

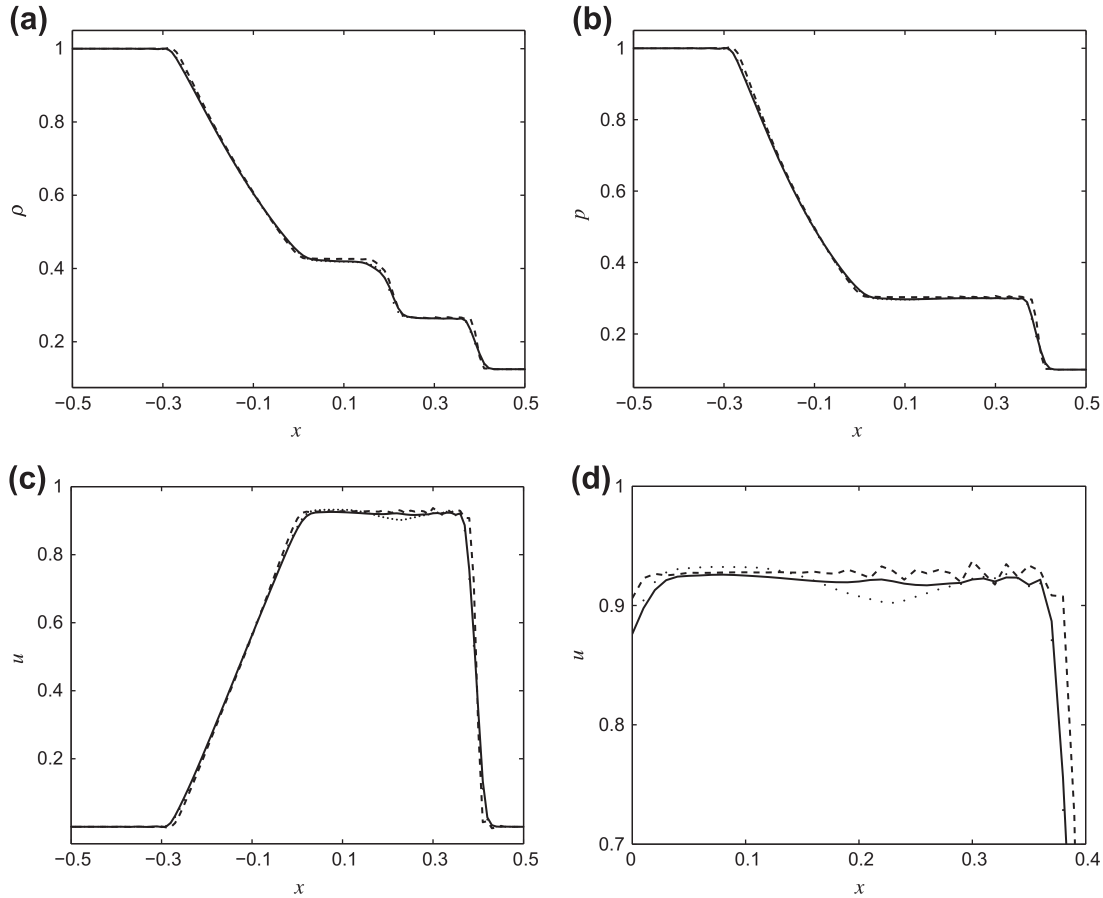

Fig. 16. Computation of the Sod's shock-tube with overlapping grids: (a) density; (b) pressure; (c) velocity; (d) zoom velocity variable: – – – single-block computation, — multi-block computation with $N_{\mathrm{order}} = 8$, ··· multi-block computation with $N_{\mathrm{order}} = 2$.

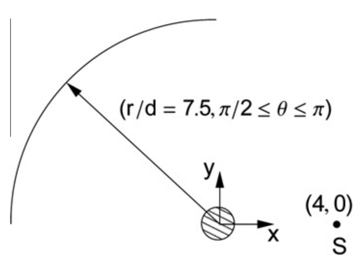

Fig. 17. Configuration for the diffraction test case: the time harmonic monopolar source is placed at point S. The directivity $D(\theta)$ will be measured on a arc at $r/d = 7.5$, $\pi/2 \leqslant \theta \leqslant \pi$.

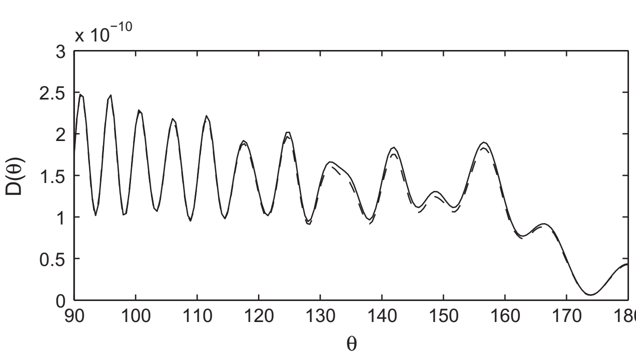

Fig. 18. Directivity $D(\theta) = r\langle p'2\rangle$ at $r/d = 7.5$: — computed solution; – – – analytical solution.

radial and azimuthal grid spacing is $\Delta r/\Delta\theta \approx 1.1$. The overset grid contains 3.2×10^5 grid points, 45% less grid points than used for the single-block computation.

Fig. 19b shows the fluctuating pressure field for the overset grid using sixth-order interpolation polynomials. Even in the near cylinder region, the diffracted field is very similar to the reference single-block computation. The acoustic waves propagate through the overlapping region without generating spurious reflections. In Fig. 20, the quantity $D(\theta, r)$ along a line defined by $\theta = \pi/2$ and $0.5 \leqslant r/d \leqslant 10$ is compared with the analytical solution for the interpolation order of 2 and 6. Using second-order polynomials leads to large discrepancies in the near cylinder region. For higher orders than six, the error made by the interpolation procedure tends to zero.

In this Section, the overset-grid approach has been successfully applied and the results compare very well with the analytical solution. The test case reveals that sixth-order Lagrangian polynomials are sufficient when acoustic perturbations are involved in order to maintain the global accuracy of the optimized 11-point finite-difference scheme.

4.7. Sound radiated by a rod-airfoil configuration

Rod-airfoil configurations are believed to be a benchmark well-suited for numerical modeling of sound generation processes in turbomachines [47]. As shown in Fig. 21, the impingement of the vortical structures in the wake of the cylinder on the leading edge of the airfoil generates sound sources. Several attempts have already been made to investigate rod-airfoil flow configurations by

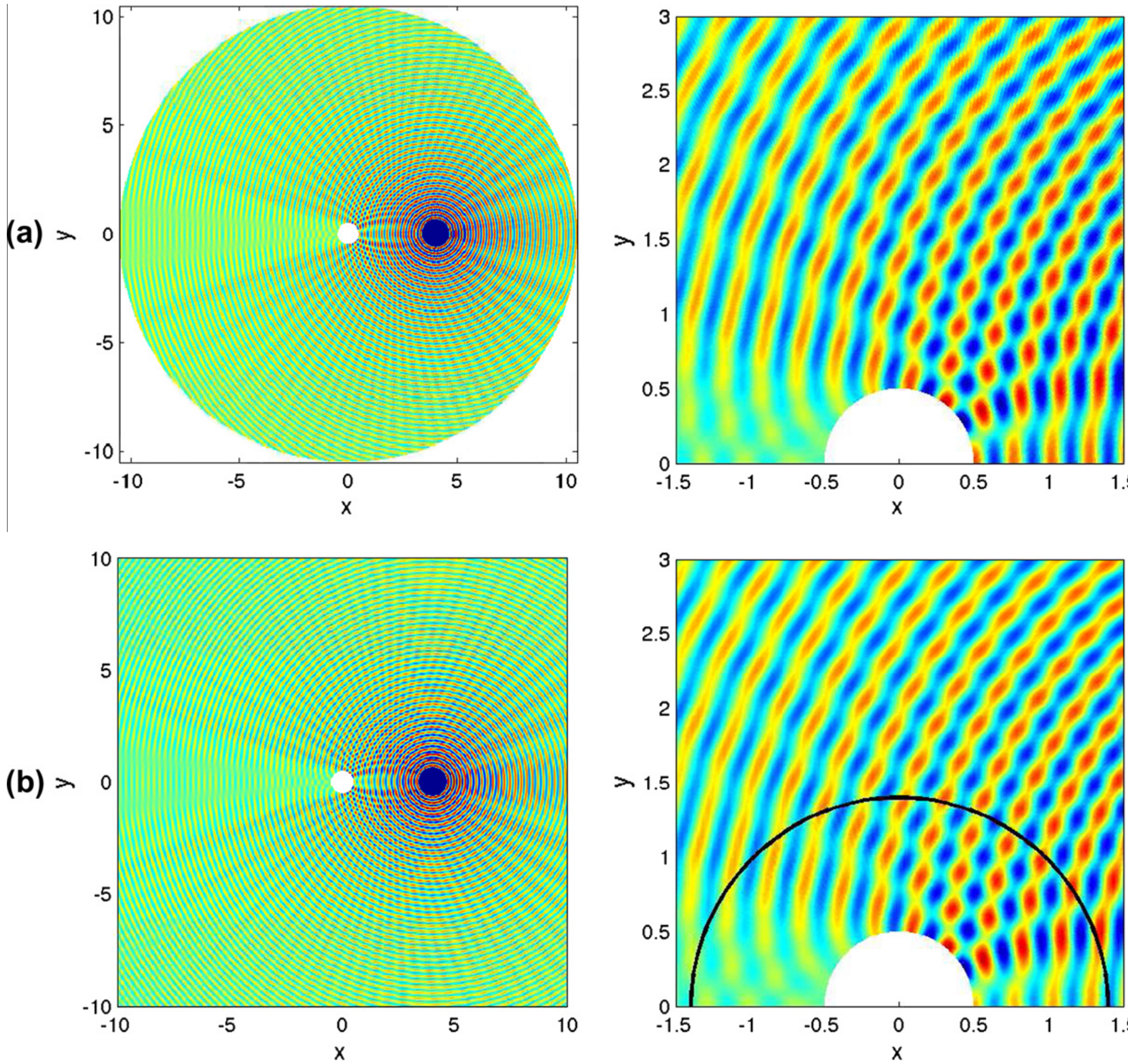

Fig. 19. Diffraction of a non-compact source by a cylinder: pressure fluctuations field (color scales $\leqslant 10^{-10}$ Pa): (a) obtained by the single-block computation; (b) obtained using overset-grid approach and sixth-order interpolation polynomials. The solid line presents the boundary of the cylindrical grid.

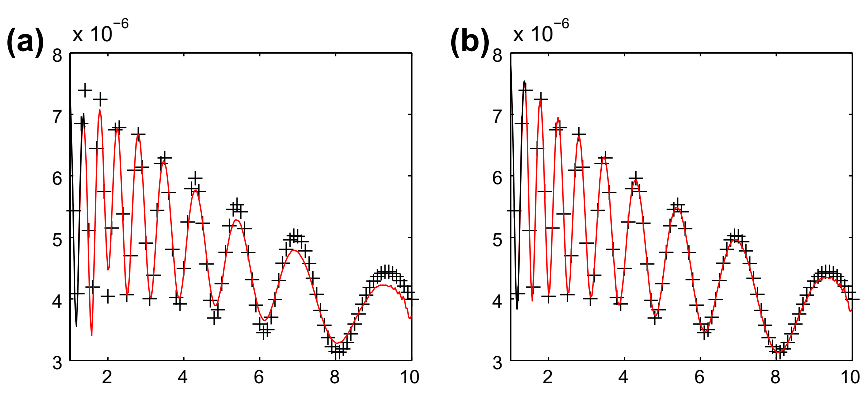

Fig. 20. Directivity $D(\theta,r)$ at $0.5 \leqslant r/d \leqslant 10$ and $\theta = \pi/2$ for different order of interpolation: (a) second-order (b) sixth-order; — computed solution; + analytical solution.

means of numerical simulations via hybrid approaches [48,49]. The direct noise calculation of this phenomena *via* LES is investigated in the present section.

The calculation aims at reproducing the features of the aerodynamic and acoustic measurements performed by Jacob et al. [47]. The flow configuration is a symmetric NACA0012 airfoil located one chord downstream a rod, whose wake contains both tonal and broadband fluctuations. The airfoil chord is equal to $c_h = 0.1$ m and the rod diameter d is taken to be a tenth of the chord length. The free-stream Mach number M_∞ is 0.2 so that the

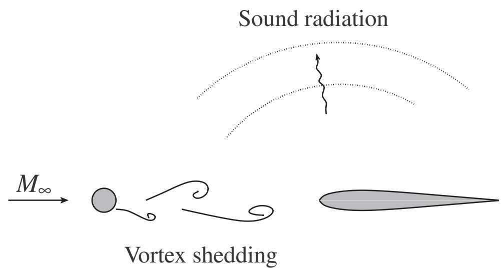

Fig. 21. Sketch of the sound generated by an airfoil interacting with the wake of a rod, placed in an uniform flow with a free-stream Mach number M_∞.

Reynolds numbers based on the chord length and the rod diameter are respectively given by $\mathrm{Re}_{c_h} = 5 \times 10^5$ and $\mathrm{Re}_d = 5 \times 10^4$. A partial view of the overset grids used for this calculation is given in Fig. 22.

As an illustration, an instantaneous snapshot of the magnitude of the velocity field, taken in the central plane of the computational domain, is presented in Fig. 23. It is seen that turbulence ignition is achieved by the rod. In particular, large scale organized structures are observed in its wake and correspond to periodic vortex shedding. Smaller turbulent scales are furthermore visible. An overview of the radiated acoustic field is in addition proposed in Fig. 23, where a snapshot of the pressure fluctuations in the central plane is plotted. A tonal noise component, associated with the periodic impingement of the rod wake on the airfoil, is clearly visible on either side of the rod-airfoil setup.

Numerical results are now compared to the experience of Jacob et al. [47] to assess the present LES. First, it should be noted that the authors pointed out that during their experiments the rod and the airfoil were not perfectly aligned. Thus, discrepancies can be expected between numerics and experience. Nonetheless, the measurements of Jacob et al. [47] are considered as references. Comparison concern both aerodynamic and aeroacoustic data.

The mean streamwise velocity $\bar{u}/U_\infty$ and the turbulent intensity $\sqrt{\overline{u'u'}}/U_\infty$ are represented in Fig. 25 as a function of the transverse coordinate y/c_h. Three streamwise locations, as shown in Fig. 24, referred to as section [A] ($x/c_h = -0.255$), section [B] ($x/c_h = 0.25$) and section [C] ($x/c_h = 1.1$) are plotted. Downstream the rod (section [A]), a good collapse between the computed mean flow value and its experimental reference is obtained. The computation overestimates the turbulent activity in the center of the wake but the overall agreement is good and few discrepancies can be seen. Further downstream, above the profile (section [B]), there is a fair agreement between the numerical and the experimental data. The calculation turns out to overestimate the streamwise mean flow and the turbulent intensity but the overall amplitude is nonetheless well predicted. Finally, the mean streamwise velocity and turbulence activity in the wake of the airfoil (section [C]), are also consistent with the experiments. Discrepancies are rather large for $y/c_h > 0$ but a very good collapse is visible for $y/c_h < 0$. Remind that

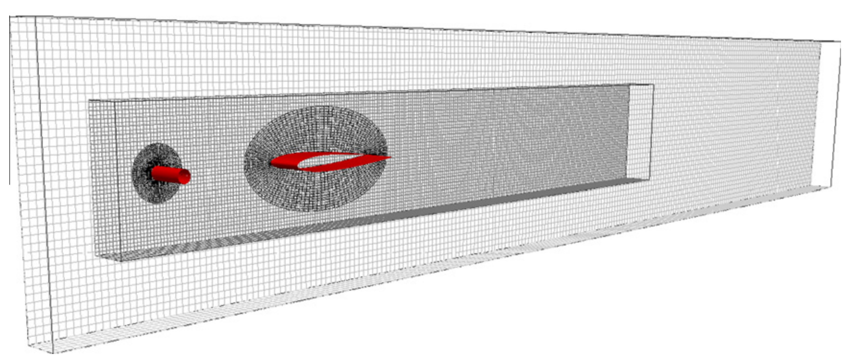

Fig. 22. 3-D view of the overset grids for the rod-airfoil configuration. Only component grids of the aerodynamic region are displayed.

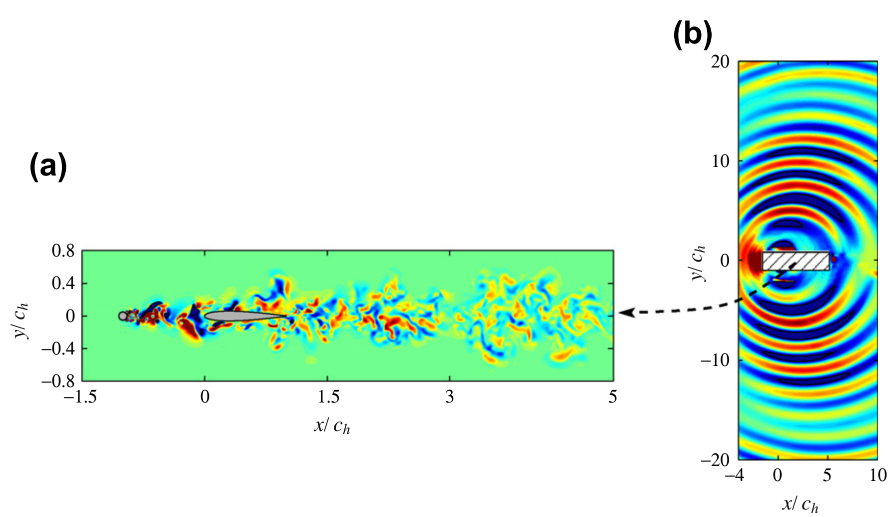

Fig. 23. (a) Snapshot of the unsteady spanwise velocity field in the central plane of the computational domain. Colorscale from $-0.2U_\infty$ (blue) to $+0.2U_\infty$ (red). Gray surfaces represent solid bodies. (b) Snapshot of the pressure fluctuations obtained in the far-field, in the central plane of the computational domain. Colorscale from −50 Pa (blue) to + 50 Pa (red). The dashed area represents the flow region represented on the left.

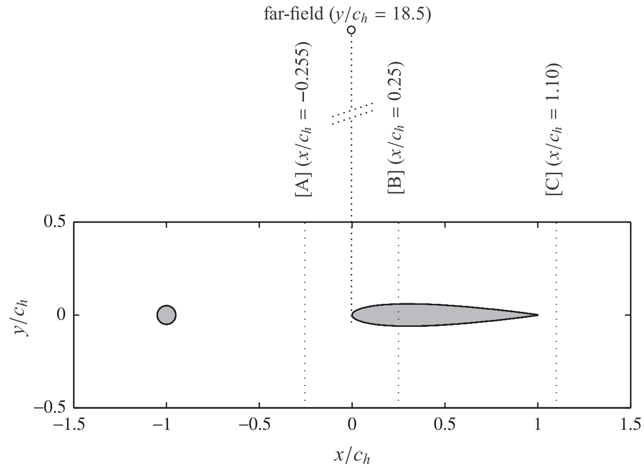

Fig. 24. Sketch of the locations for the measurements of pressure and velocities.

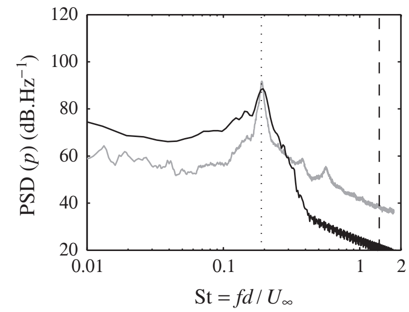

Fig. 26. Power spectral density of the pressure perturbations measured in the far-field for an observer normal to the flow at a distance $R = 18.5c_h$ from the airfoil leading edge. The present LES results (black plot) are compared to the data provided by the experiments of Jacob et al. [47] (gray plot). The dotted line indicates the expected Strouhal number St = 0.19 of the vortex-shedding frequency behind the cylinder. The dashed line represents the mesh cut-off Strouhal number St = 1.39 in the far-field grid.

the experimental setup is not symmetric so that the hot-wire measurements are consequently not symmetric too.

The power spectral density (PSD) of the far-field pressure fluctuations at the location $(x/c_h, y/c_h) = (0, 18.5)$ is provided in Fig. 26 as a function of the Strouhal number $\mathrm{St} = fd/U_\infty$ based on the cylinder diameter. A good collapse between numerical and experimental results is observed even though the half-width of the peak is overestimated. This trend is likely to be due to the

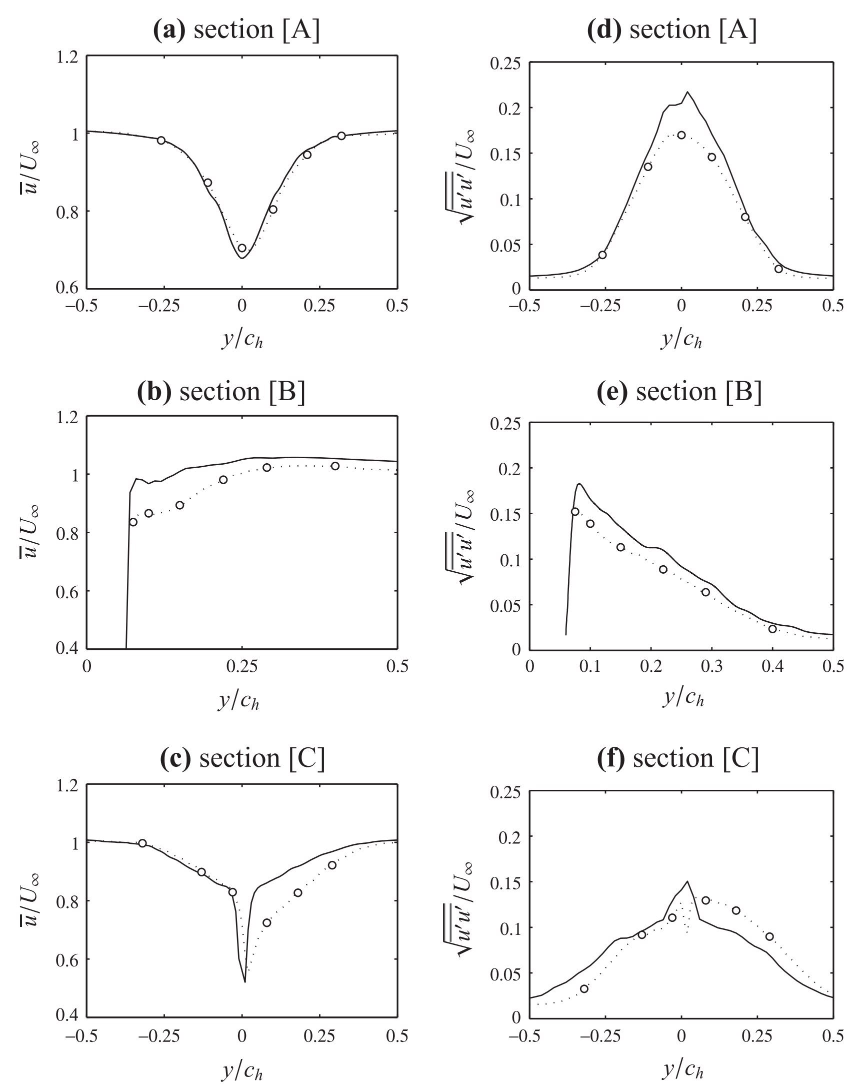

Fig. 25. **(a–c)** Mean streamwise velocity $\overline{u}/U_\infty$ as a function of the transverse position y/c_h, and **(d–f)**, mean streamwise turbulent intensity $\sqrt{\overline{u'u'}}/U_\infty$ as a function of the transverse position y/c_h, for various streamwise locations. —, present LES; ···○···, experimental data [47].

discrepancies between the length of the signals of the simulation and of the experiments. Numerical calculation indeed provide relatively short time-resolved data. Nonetheless, as expected, the calculated spectrum exhibit a strong tonal component at the vortex shedding frequency and the predicted Strouhal number shows a very good agreement with the reference data. In addition the pressure level radiated by the harmonic peak is well reproduced. The gap between the simulation and the experiments remains small, about 4 dB.

More details can be found in [50]. In addition, a detailed analysis of the influence of the distance between the rod and the airfoil on the flow and the acoustic field can be found in [51].

5. Conclusion and future plans

A numerical method has been described for performing compressible LES in CAA applications. The algorithm is based on a high-order explicit finite-difference scheme in conjunction with a spatial low-pass filter. Non-linear filters are used to capture discontinuities in compressible flows. In order to address complex geometrical configurations, overlapping grids are used and the communications between domains are performed via high-order Lagrangian interpolation. The validation procedure has illustrated the ability of the algorithm to capture discontinuities without damaging its spectral behavior. The high-order overset-grid technique has preserved the algorithm accuracy on both classical CFD and CAA applications. Moreover, comprehensive studies can be performed, as shown by the rod-airfoil configuration, which can help understanding the flow physics of sound generation processes in turbulent flows. The present numerical approach appears to provide a robust and accurate tool for performing LES of realistic compressible flows for CAA applications.

A detailed validation procedure is in progress to check the accuracy of the present algorithm for moving grids. To address fluid/structure interaction, the coupling between flow patterns and structure dynamics will be studied with the aim of preserving the high-order accuracy of the present solver. The choice of the time integration method is also to be considered. In an explicit method as used in this work, the time step is imposed by stability constraints. However, the time step needed to respect the physical time scales of the turbulent flow may be larger. This is the case for turbulent wall-bounded flows, for example. The use of implicit time integration method would make it possible to circumvent the numerical stability by using a time step only driven by the flow physics [30,52].

Acknowledgments

This work is supported by the “Agence Nationale de la Recherche” under the reference ANR-06-CIS6-011. The authors thank Dr. Bill Henshaw for his valuable recommendations concerning the overset-grid strategy.

Appendix A. Scheme and filter coefficients

See Tables A.3 and A.4.

Table A.3
Coefficients of the FD schemes and of the low-pass filters: (a) 11-point coefficients proposed by Bogey and Bailly [10]; (b) standard 7-point coefficients.

(a)			
s_0	0.0	d_0	0.2150448841109084
s_1	0.872756993962667	d_1	−0.1877728835894673
s_2	−0.286511173973333	d_2	0.1237559487873421
s_3	0.090320001280000	d_3	−0.0592275755757438
s_4	−0.020779405824000	d_4	0.0187216091572037
s_5	0.002484594688000	d_5	−0.0029995408347887
(b)			
s_0	0.0	d_0	5/16
s_1	3/4	d_1	−15/64
s_2	−3/20	d_2	3/32
s_3	1/60	d_3	−1/64

Table A.4
(a) Standard RK4 coefficients; (b) coefficients of the optimized second-order filter proposed by Bogey et al. [38].

(a)	
α_1	1/4
α_2	1/3
α_3	1/2
α_4	1
(b)	
c_1	−0.210383
c_2	0.039617

Appendix B. Finite-volume formulation of the finite-difference scheme

In a similar way as Popescu et al. [53], a finite-difference scheme can be recasted in a finite-volume framework. We consider the following non-linear conservation law:

$$\partial_t u + \partial_x f(u) = 0. \tag{B.1}$$

A finite-difference scheme can be written in the classical form:

$$\partial_x f(u)|_i \approx \frac{1}{\Delta x} \sum_{m=-r}^{q} s_m f(u_{i+m}).$$

On the other hand, a finite-volume discretization leads to:

$$\frac{\mathrm{d}}{\mathrm{d}t} \int_{x_{i-1/2}}^{x_{i+1/2}} u(x,t)\mathrm{d}x + f_{i+1/2} - f_{i-1/2} = 0.$$

Thus, a finite-volume formulation of the finite-difference scheme is:

$$\sum_{m=-r}^{q} s_m f(u_{i+m}) = f_{i+1/2} - f_{i-1/2},$$

with

$$f_{i+1/2} = \sum_{m=-r+1}^{q} \beta_m f(u_{i+m}).$$

Finally, the finite-volume coefficient β_m can be expressed using the finite-difference ones:

$$\begin{cases} \beta_q = s_q \\ \beta_m - \beta_{m+1} = s_m - r + 1 \leqslant m \leqslant q-1 \\ \beta_{-r} = s_{-r} \end{cases}$$

References

[1] Lafon P, Caillaud S, Devos J-P, Lambert C. Aeroacoustical coupling in a ducted shallow cavity and fluid/structure effects on a steam line. J Fluids Struct 2003;18(6):695–713.
[2] Meier GEA, Szumowski AP, Selerowicz WC. Self-excited oscillations in internal transonic flows. Prog Aerospace Sci 1990;27(2):145–200.
[3] Colonius T, Lele SK. Computational aeroacoustics: progress on nonlinear problems on sound generation. Prog Aerospace Sci 2004;40:345–416.
[4] Bailly C, Bogey C, Marsden O. Progress in direct noise computation. Int J Aeroacoust 2010;9(1–2):123–43.
[5] Ekaterinaris JA. High-order accurate, low numerical diffusion methods for aerodynamics. Prog Aerospace Sci 2005;41:192–300.
[6] Jiang G-S, Shu C-W. Efficient implementation of weighted ENO schemes. J Comput Phys 1996;126(1):202–28.

[7] Cockburn B, Karniadakis GE, Shu C-W. Discontinuous Galerkin methods. Berlin: Springer; 1999.
[8] Lele SK. Compact finite difference schemes with spectral-like resolution. J Comput Phys 1992;103(1):16–42.
[9] Tam CKW, Webb JC. Dispersion-relation-preserving finite differences schemes for computational acoustics. J Comput Phys 1993;107(2):262–81.
[10] Bogey C, Bailly C. A family of low dispersive and low dissipative explicit schemes for flow and noise computations. J Comput Phys 2004;194(1):194–214.
[11] Marsden O, Bogey C, Bailly C. High-order curvilinear simulations of flows around non-Cartesian bodies. J Comput Acoust 2005;13(4):731–48.
[12] Visbal MR, Gaitonde DV. On the use of higher-order finite-difference schemes on curvilinear and deforming meshes. J Comput Phys 2002;181(1):155–85.
[13] Delfs JW. An overlapped grid technique for high resolution CAA schemes for complex geometries, AIAA Paper 2001-2199.
[14] Desquesnes G, Terracol M, Manoha E, Sagaut P. On the use of a high order overlapping grid method for coupling in CFD/CAA. J Comput Phys 2006;220(1):355–82.
[15] Sherer SE, Scott JN. High-order compact finite-difference methods on general overset grids. J Comput Phys 2005;210(2):459–96.
[16] Rizzetta DP, Visbal MR, Morgan PE. A high-order compact finite-difference scheme for large-eddy simulation of active flow control. Prog Aerospace Sci 2008;44(6):397–426.
[17] Vinokur M. Conservation equations of gasdynamics in curvilinear coordinate systems. J Comput Phys 1974;14(105):48–56.
[18] Viviand H. Formes conservatives des équations de la dynamique des gaz. La Recherche Aérospatiale 1974;158:65–6.
[19] Zhang H, Reggio M, Trépanier JY, Camarero R. Discrete form of the GCL for moving meshes and its implementation in CFD schemes. Comput Fluids 1993;22(1):9–23.
[20] Thomas PD, Lombard CK. Geometric conservation law and its application to flow computations on moving grids. AIAA J 1979;17(10):1030.
[21] Bogey C, Bailly C. Large eddy simulations of transitional round jets: influence of the Reynolds number on flow development and energy dissipation. Phys Fluids 2006;213(2):777–802.
[22] Bogey C, Bailly C. An analysis of the correlations between the turbulent flow and the sound pressure fields of subsonic jets. J Fluid Mech 2007;583:71–97.
[23] Berland J, Bogey C, Bailly C. Low-dissipation and low-dispersion fourth-order Runge–Kutta algorithm. Comput Fluids 2006;35(10):1459–63.
[24] Hirsch C. Numerical computation of internal and external flows. New-York: J. Wiley and Sons; 1988.
[25] Bogey C, Bailly C. Turbulence and energy budget in a self-preserving round jet: direct evaluation using large-eddy simulation. J Fluid Mech 2009;627:129–60.
[26] Vreman AW, Geurts BJ, Kuerten JG. A priori tests of large-eddy simulation of compressible plane mixing layer. J Eng Math 1995;118(1):24–37.
[27] Berland J, Bogey C, Bailly C. Numerical study of screech generation in a planar supersonic jet. Phys Fluids 2007;19(075105):1–14.
[28] Emmert T, Lafon P, Bailly C. Numerical study of self-induced transonic flow oscillations behind a sudden duct enlargement. Phys Fluids 2009;21(106105):1–15.
[29] Marsden O, Bogey C, Bailly C. Direct noise computation of the turbulent flow around a zero-incidence airfoil. AIAA J 2008;46(4):874–83.
[30] Rizzetta DP, Visbal MR, Blaisdell GA. A time-implicit high-order compact differencing and filtering scheme for large-eddy simulation. Int J Numer Meth Fluids 2003;42(6):665–93.
[31] Berland J, Lafon P, Daude F, Crouzet F, Bogey C, Bailly C. Filter shape dependence and effective scale separation in large-eddy simulations based on relaxation filtering. Comput Fluids 2011;47(1):65–74.
[32] Yee HC, Sandham ND, Djomehri MJ. Low-dissipative high-order shock capturing methods using characteristic-based filters. J Comput Phys 1999;150(1):199–238.
[33] Kim JW, Lee DJ. Adaptive nonlinear artificial dissipation model for computational aeroacoustics. AIAA J 2001;39(5):810–8.
[34] Moase WH, Brear MJ, Manzie C. The forced response of choked nozzles and supersonic diffusers. J Fluid Mech 2007;585:281–304.
[35] Jameson A, Schmidt W, Turkel E. Numerical solution of the Euler equations by finite volume methods using Runge–Kutta time-stepping schemes, AIAA Paper 81-1259.
[36] Garnier E, Mossi M, Sagaut P, Comte P, Deville M. On the use of shock-capturing schemes for large-eddy simulation. J Comput Phys 1999;153(2):273–311.
[37] Ducros F, Ferrand V, Nicoud F, Weber C, Darracq D, Gacherieu C, et al. Large-eddy simulation of the shock/turbulence interaction. J Comput Phys 1999;152(2):517–49.
[38] Bogey C, de Cacqueray N, Bailly C. A shock-capturing methodology based on adaptive spatial filtering for high-order non-linear computations. J Comput Phys 2009;228(5):1447–65.
[39] Visbal MR, Gaitonde DV. Shock capturing using compact-differencing-based methods, AIAA Paper 2005-1265.
[40] Henshaw WD. Ogen: an overlapping grid generator for overture, Tech. Rep. UCRL-MA-132237, Lawrence Livermore National Laboratory; 1998.
[41] Tam CKW, Kurbatskii KA. A wavenumber based extrapolation and interpolation method for use in conjunction with high-order finite difference schemes. J Comput Phys 2000;157(2):588–617.
[42] Berland J, Bogey C, Marsden O, Bailly C. High-order, low dispersive and low dissipative explicit schemes for multiple-scale and boundary problems. J Comput Phys 2007;224(2):637–62.
[43] Thompson KW. Time-dependent boundary conditions for hyperbolic systems, II. J Comput Phys 1990;89(2):439–61.
[44] Bogey C, Bailly C. Three-dimensional non-reflective boundary conditions for acoustic simulations: far field formulation and validation test cases. Acta Acust 2002;88(4):463–71.
[45] Woodward PR, Colella P. The numerical simulation of two-dimensional fluid flow with strong shocks. J Comput Phys 1984;54(1):115–73.
[46] Tam CKW, Hardin JC, editors, Second computational aeroacoustics (CAA) workshop on benchmark problems, NASA CP-3352; 1997.
[47] Jacob MC, Boudet J, Casalino D, Michard M. A rod-airfoil experiment as benchmark for broadband noise modeling. J Theoret Comput Fluid Dyn 2005;19(3):171–96.
[48] Boudet J, Grosjean N, Jacob MC. Wake-airfoil interaction as broadband noise source: a large-eddy simulation study. Int J Aeroacoust 2005;4(1):93–116.
[49] Greschner B, Thiele F, Jacob MC, Casalino D. Prediction of sound generated by a rod-airfoil configuration using EASM DES and the generalised Lighthill/FW-H analogy. Comput Fluids 2008;37(4):402–13.
[50] Berland J, Lafon P, Crouzet F, Daude F, Bailly C. Numerical insight into sound sources of a rod-airfoil flow configuration using direct noise calculation, AIAA Paper 2010-3705.
[51] Berland J, Lafon P, Crouzet F, Daude F, Bailly C. A parametric study of the noise radiated by the flow around multiple bodies: direct noise computation of the influence of the separating distance in rod-airfoil flow configurations, AIAA Paper 2011-2819.
[52] Daude F, Mary I, Comte P. Implicit time integration method for LES of complex flows. In: Direct and large-eddy simulation VI. Springer; 2006. p. 771–8.
[53] Popescu M, Shyy W, Garbey M. Finite volume treatment of dispersion-relation-preserving and optimized prefactored compact schemes for wave propagation. J Comput Phys 2005;210(2):705–29.